Available online at www.sciencedirect.com
SCIENCE DIRECT®
PERGAMON
Planetary and Space Science 51 (2003) 541–561
Planetary and Space Science
www.elsevier.com/locate/pss

Analysis of entry accelerometer data: A case study of Mars Pathfinder

Paul Withers[a,*], M.C. Towner[b], B. Hathi[b], J.C. Zarnecki[b]

[a] *Lunar and Planetary Laboratory, University of Arizona, Tucson, AZ 85721, USA*
[b] *Planetary and Space Science Research Institute, Open University, Walton Hall, Milton Keynes, MK7 6AA, UK*

Received 19 August 2002; received in revised form 6 March 2003; accepted 5 May 2003

Abstract

Accelerometers are regularly flown on atmosphere-entering spacecraft. Using their measurements, the spacecraft trajectory and the vertical structure of density, pressure, and temperature in the atmosphere through which it descends can be calculated. We review the general procedures for trajectory and atmospheric structure reconstruction and outline them here in detail. We discuss which physical properties are important in atmospheric entry, instead of working exclusively with the dimensionless numbers of fluid dynamics. Integration of the equations of motion governing the spacecraft trajectory is carried out in a novel and general formulation. This does not require an axisymmetric gravitational field or many of the other assumptions that are present in the literature. We discuss four techniques—*head-on*, *drag-only*, *acceleration ratios*, and *gyroscopes*—for constraining spacecraft attitude, which is the critical issue in the trajectory reconstruction. The *head-on* technique uses an approximate magnitude and direction for the aerodynamic acceleration, whereas the *drag-only* technique uses the correct magnitude and an approximate direction. The *acceleration ratios* technique uses the correct magnitude and an indirect way of finding the correct direction and the *gyroscopes* technique uses the correct magnitude and a direct way of finding the correct direction. The *head-on* and *drag-only* techniques are easy to implement and require little additional information. The *acceleration ratios* technique requires extensive and expensive aerodynamic modelling. The *gyroscopes* technique requires additional onboard instrumentation. The effects of errors are briefly addressed. Our implementations of these trajectory reconstruction procedures have been verified on the Mars Pathfinder dataset. We find inconsistencies within the published work of the Pathfinder science team, and in the PDS archive itself, relating to the entry state of the spacecraft. Our atmospheric structure reconstruction, which uses only a simple aerodynamic database, is consistent with the PDS archive to about 4%. Surprisingly accurate profiles of atmospheric temperatures can be derived with no information about the spacecraft aerodynamics. Using no aerodynamic information whatsoever about Pathfinder, our profile of atmospheric temperature is still consistent with the PDS archive to about 8%. As a service to the community, we have placed simplified versions of our trajectory and atmospheric structure computer programmes online for public use.

Keywords: Accelerometer; Atmosphere; Atmospheric entry; Data reduction techniques; Mars; Mars Pathfinder

1. Introduction

1.1. Uses of accelerometers in spaceflight

An accelerometer instrument measures the linear, as opposed to angular, accelerations experienced by a test mass. When rigidly mounted inside a spacecraft and flown into space, an accelerometer instrument measures aerodynamic forces and additional contributions from any spacecraft thruster activity or angular motion of the test mass about the spacecraft's centre of mass (Tolson et al., 1999). The gravitational force acting on the spacecraft's centre of mass cannot be detected by measurements made in a frame fixed with respect to the spacecraft, since the spacecraft, accelerometer instrument, and test mass are all free falling at the same rate. In practice, three-dimensional acceleration measurements are synthesised from three orthogonal one-dimensional acceleration measurements, each measured by a different instrument with inevitably slightly different properties. Instrument biases, sampling rates, digitisation errors, and so on also affect the accelerometer measurement.

When a spacecraft passes through the atmosphere of a planetary body, it will experience aerodynamic forces in addition to gravity. These forces will affect the spacecraft's trajectory. The gravitational acceleration is usually known as a function solely of position from a pre-existing gravity

* Corresponding author. Center for Space Physics, 725 Commonwealth Avenue, Boston, MA 02215, USA. Fax: +1-520-621-4933.
E-mail address: withers@lpl.arizona.edu (P. Withers).

0032-0633/03/$ - see front matter © 2003 Elsevier Ltd. All rights reserved.
doi:10.1016/S0032-0633(03)00077-1

Nomenclature

A	area
$\underline{a}$	the linear acceleration vector of the centre of mass of the rigid body
aero	subscript indicating effects due to aerodynamics
$\underline{B}$	an arbitrary vector
C	a dimensionless force coefficient
C_{20}	the tesseral normalised spherical harmonic coefficient of degree 2 and order 0
cart	subscript for a Cartesian co-ordinate system
$\underline{\underline{EM}}$	Euler matrix in Goldstein's xyz-convention
$\underline{F}_{\text{aero}}$	aerodynamic force acting on the spacecraft
$\underline{g}$	the acceleration vector due to gravity
GM	the product of the gravitational constant and the mass of the planet
inert	subscript for an inertial frame
Kn	Knudsen number
m	mass
m_{mol}	mean molecular mass
Ma	Mach number
mom	subscript for a momentary frame (defined in the text)
p	atmospheric pressure
$P_{20}(x)$	the normalised associated Legendre function of degree 2 and order 0, $P_{20}(x) \propto \frac{1}{2}(3x^2-1)$
$\underline{r}$	a position vector
r_{ref}	a reference radius within $U(\underline{r})$. It is often, but not necessarily, the mean or mean equatorial planetary radius. It has meaning only in association with the spherical harmonic coefficients.
r, θ, ϕ	spherical polar position co-ordinates or subscripts indicating direction
Re	Reynolds number
sct	subscript for a spacecraft-fixed frame
sph	subscript for a spherical polar co-ordinate system
T	atmospheric temperature
t	time
$U(\underline{r})$	the gravitational potential at position $\underline{r}$
V	the speed of the rigid body relative to the surrounding fluid
$\underline{v}$	the velocity vector of the centre of mass of the rigid body
v_{entry}	an entry speed
$\underline{v}_{\text{rel}}$	velocity of the centre of mass of the rigid body relative to the atmosphere
$\underline{v_{wind}}$	velocity of the atmosphere due to planetary rotation
x, y, z	Cartesian position co-ordinates or subscripts indicating direction

Greek letters

α, β	two angles necessary to define spacecraft attitude
γ	flight path angle below the horizontal
γ_{fluid}	ratio of specific heats of a fluid
η	dynamic viscosity
θ	colatitude, the angle between the z-axis and $\underline{r}$
ρ	fluid density
ϕ	east longitude, the angle between the x-axis and the projection of $\underline{r}$ into the xy-plane. ϕ is measured in the sense of a positive rotation about the z-axis rotating the x-axis onto the projection of $\underline{r}$ into the xy-plane
$\phi_{\text{Euler}}, \psi_{\text{Euler}}, \theta_{\text{Euler}}$	Euler angles
ψ	flight path azimuth measured clockwise from north
Ω	the angular velocity of the spacecraft
ω	the planetary rotation rate

model for the planetary body. In the absence of an atmosphere, the spacecraft trajectory can be calculated accurately from that alone. However, the presence of an atmosphere and consequent aerodynamic forces causes the spacecraft's trajectory to differ from the gravity-only case. Additional measurements are needed to define accurately the spacecraft's trajectory. Onboard accelerometer measurements of the aerodynamic acceleration of the spacecraft can be combined with the gravity model to give the total acceleration experienced by the spacecraft. The equations of motion can then be integrated to reveal the spacecraft's modified trajectory.

If the spacecraft is merely passing, or aerobraking, through a planetary atmosphere, then the accelerometer measurements can be analysed later, upon transmission to Earth, for the trajectory analysis and to reveal properties of the atmosphere (e.g. Tolson et al., 1999). If the spacecraft is actively reacting to the forces acting on it to reach a desired orbit, such as some aerocapture scenarios, then the accelerometer data must be used in real-time onboard the spacecraft (e.g. Wercinski and Lyne, 1994). If the spacecraft is a planetary lander or entry probe approaching the surface or interior of the planetary body and needs to prepare for landing or deploy sensors intended for lower atmosphere

use only, then the accelerometer data can also be used in real-time onboard the spacecraft (e.g. Tu et al., 2000). The accelerometer data are not absolutely necessary for this; if there is sufficient confidence in a model of the planetary atmosphere, a timer-based approach can be used instead. However, this is rarely used due to the increased risk.

An atmosphere-entering spacecraft must carry an accelerometer for its trajectory to be known and, for landers and entry probes, to control its entry, descent, and possible landing, although radar altimetry and other techniques can also control parts of the entry. These are the operational uses of accelerometer data. Scientific uses are also important.

1.2. Fluid dynamics and atmospheric entry

The forces and torques acting on a rigid body, such as a spacecraft, traversing a fluid region, such as an atmosphere, are, in principle, completely constrained given the size, shape, and mass of the rigid body, its orientation, the far-field speed of the fluid with respect to the rigid body, the composition of the fluid, and the thermodynamic state of the fluid (Landau and Lifshitz, 1956, 1959, 1960). Specifying the thermodynamic state of a fluid requires two intensive thermodynamic variables, such as density and pressure. As an inverse problem, knowledge of the forces and torques acting on a rigid body, physical characteristics of the rigid body, flow velocity, and fluid composition is just one relationship short of completely constraining the thermodynamic state of the fluid.

When a spacecraft is much smaller than the volume of the atmosphere, its passage has no effect on atmospheric bulk properties. The atmosphere continues to obey the same laws of conservation of mass, momentum, and energy that it did prior to the arrival of the spacecraft. Conservation of momentum in a gravitational field provides a relationship between the fluid density and pressure (Landau and Lifshitz, 1959). This additional relationship supplies the needed final constraint.

Measurements of the aerodynamic forces and torques acting on a spacecraft can uniquely define both the atmospheric density and pressure along the spacecraft trajectory. Using an appropriate equation of state reveals the corresponding atmospheric temperature. Linear and angular acceleration measurements can be converted into forces and torques using the known spacecraft mass and moments of inertia.

Practical application, with the appropriate equations, of this abstract physical reasoning will follow later. For now, it is enough that we demonstrate that a unique solution exists. Accelerometer data can define profiles of atmospheric density, pressure, and temperature along the spacecraft trajectory, *provided* the aerodynamic properties of the spacecraft are known sufficiently well. These profiles are of great utility to atmospheric scientists.

1.3. Flight heritage

Accelerometers have successfully flown on the following entry probes/landers: planetary atmosphere experiments test vehicle (PAET), Mars 6, both Viking landers, the 4 Pioneer Venus probes, Veneras 8–14, the Space Shuttle, the Galileo probe, and Mars Pathfinder (Seiff et al., 1973, 1980, 1998; Kerzhanovich, 1977; Seiff and Kirk, 1977; Avduevskii et al., 1983a, b; Blanchard et al., 1989; Magalhães et al., 1999). Accelerometers have successfully been used in the aerobraking of Atmosphere Explorer-C and its successors at Earth, Mars Global Surveyor, and Mars Odyssey (Marcos et al., 1977; Keating et al., 1998). Atmospheric drag at Venus was studied without using accelerometers on both Pioneer Venus Orbiter and Magellan (Strangeway, 1993; Croom and Tolson, 1994). Failed planetary missions involving accelerometers include Mars 7, Mars 96, Mars Polar Lander, Deep Space 2, and Mars Climate Orbiter. Upcoming missions involving accelerometers include Beagle 2 and NASA's Mars Exploration Rovers for the 2003 Mars launch opportunity, and Huygens, currently on its way to Titan (Lebreton et al., 1994; Sims et al., 1999; Squyres, 2001).

2. Equations of motion

2.1. Previous work

The aim of the trajectory integration is to reconstruct the spacecraft's position and velocity as a function of time. Although it is easy to understand the concept of trajectory integration as "sum measured aerodynamic accelerations and known gravitational accelerations, then integrate forward from known initial position and velocity," it is more challenging to actually perform the integration. The primary complications are that aerodynamic accelerations are measured in the frame of the spacecraft, but the equations of motion are simplest in an inertial frame and the final trajectory is most usefully expressed in a rotating frame fixed to the surface of the planetary body.

Many of the publications in this field provide specific equations for the trajectory reconstruction as applied to their work. Of these, most neglect planetary rotation or include only the radial component of the gravitational field (Seiff, 1963; Peterson, 1965a, b; Sommer and Yee, 1969; Seiff et al., 1973). The trajectory reconstruction work for the Viking landers includes only the radial component of the gravitational field (Seiff and Kirk, 1977), whereas the trajectory reconstruction work for the Pioneer Venus probes does not provide specific equations (Seiff et al., 1980). Galileo probe trajectory reconstruction introduced the concept of changing frames between each integration step to remove the Coriolis and centrifugal forces (Seiff et al., 1998). The trajectory reconstruction integration for Pathfinder was performed in a planet-centred spherical co-ordinate system

rotating with the planet (Magalhães et al., 1999). These assumptions are often valid, but we wish to describe a general technique for performing the trajectory integration. Individual cases can then be examined for terms that can be neglected.

2.2. Alternative formulation

We have elected not to perform the trajectory integration in the rotating, planet-fixed frame. Instead, we perform the integration in an inertial frame. To express the trajectory in a rotating, planet-fixed frame, we followed the work of the Galileo trajectory reconstruction and used different intermediate frames at each timestep (Seiff et al., 1998). These intermediate frames are instantaneously coincident with a rotating, planet-fixed frame at the relevant point in time. Since the integration of the equations of motion is being performed in an inertial frame, there is no need for the Coriolis or centrifugal forces. Vector positions, velocities, and accelerations can be transformed between frames with standard techniques. These frame transformations do not require the Coriolis or centrifugal forces either. This formulation will not encourage an analytical solution, but this is not a great loss since any realistic trajectory integration will be performed numerically. Thus, we introduce two sets of reference frames, *inertial* and *momentary*, in both *Cartesian* and *spherical* polar co-ordinate systems.

2.3. Co-ordinate systems and frames

We define an *inertial Cartesian frame* as a right-handed Cartesian co-ordinate system with its origin at the centre of mass of a planet and z-axis aligned with the planetary rotation axis, with the positive x-axis to pass through the rotating planet's zero east longitude line at time $t = 0$. The y-axis completes a right-handed set. One can then construct the usual spherical polar co-ordinate system about this set. This is the *inertial spherical frame*. Most introductory mechanics or applied mathematics textbooks, such as Arfken and Weber (1995), have diagrams of these frames and their co-ordinates. We then define the *momentary spherical frame*: we use the magnitude of $\underline{r}$, r_{mom}, a colatitude referenced to the surface of the planet, θ_{mom}, and an east longitude referenced to the surface of the planet, ϕ_{mom}, as a spherical co-ordinate frame. At any time t, it is non-rotating and transformations between it and the *inertial Cartesian frame* do not need to consider fictitious Coriolis and centrifugal forces. An instant later, as the planet has rotated slightly, this frame is removed and redefined so that colatitudes and east longitudes once again match up with surface features. It is not a rotating frame, it only exists for an instant, and so only instantaneous transformations between it and other frames can be made. No integration with time can be done in this frame because it does not exist for the duration of a timestep. One can then use the *momentary spherical frame* to construct a Cartesian co-ordinate system with the usual conventions. This also only exists for an instant and no integration with time can be done in this frame. This is the *momentary Cartesian frame*.

2.4. Transformations between frames

There are many different conventions for defining latitude and east longitude on the surface of a planet. Geographic, geodetic, and geocentric are some of the more well-known ones that are applied to the Earth (Lang, 1999). We shall assume that all latitudes and east longitudes referenced to the surface of the planet are in a planetocentric system. We use the east-positive planetocentric system for mathematical convenience, as was used for Galileo, Mars Global Surveyor, and Pathfinder. Care must be taken when comparing data to older planetary data products which may use a west-positive planetographic system.

Consider an arbitrary vector $\underline{B}$:

$$\underline{B} = B_x\underline{\hat{x}} + B_y\underline{\hat{y}} + B_z\underline{\hat{z}} = B_r\underline{\hat{r}} + B_\theta\underline{\hat{\theta}} + B_\phi\underline{\hat{\phi}}. \tag{1}$$

Expressions for the unit vectors of one frame in terms of the other frame's unit vectors are needed to transform $\underline{B}$ between *spherical* and *Cartesian* frames. These are given in, for example, Chapter 2 of Arfken and Weber (1995). These apply to transformations between the two *momentary* frames and transformations between the two *inertial* frames.

Finally, we need a transformation for $\underline{B}$ between the *momentary* and *inertial* frames.

The *momentary Cartesian* and *inertial Cartesian* frames are related as follows:

$$\underline{\hat{x}}_{\mathrm{inert}} = \underline{\hat{x}}_{\mathrm{mom}}\cos(\omega t) - \underline{\hat{y}}_{\mathrm{mom}}\sin(\omega t), \tag{2a}$$

$$\underline{\hat{y}}_{\mathrm{inert}} = \underline{\hat{x}}_{\mathrm{mom}}\sin(\omega t) + \underline{\hat{y}}_{\mathrm{mom}}\cos(\omega t), \tag{2b}$$

$$\underline{\hat{z}}_{\mathrm{inert}} = \underline{\hat{z}}_{\mathrm{mom}}. \tag{2c}$$

It is now possible to transform any vector quantity, such as a position, velocity, or acceleration, between all the four frames. We have assumed that the centre of mass of the planet is at rest in some inertial frame. Its motion around the Sun and other motions, such as the motion of the solar system, are neglected. The resultant error is small and can easily be quantified.

2.5. Solution procedure for the gravity-only case

In an *inertial* frame, the equations of motion of the centre of mass of a rigid body, the spacecraft, are:

$$\dot{\underline{r}} = \underline{v}, \tag{3a}$$

$$\dot{\underline{v}} = \underline{a}. \tag{3b}$$

If the only force acting on the centre of mass of the rigid body is gravity due to the nearby planet, then

$$\underline{a} = \underline{g}(\underline{r}) = \nabla U(\underline{r}), \tag{4}$$

where $\underline{g}(\underline{r})$ does not include any centrifugal component since we are working in an inertial frame. Here we expand $U(\underline{r})$ only to second degree and order (e.g. Smith et al., 1993). There are many conventions for spherical harmonic expansions. We use that of Lemoine et al. (2001) which follows Kaula (1966) in that $P_{20}(1) = \sqrt{5}$. The normalisation convention for C_{20} must be consistent with that for $P_{20}(x)$:

$$U(\underline{r}) = \frac{GM}{r_{\text{mom}}}\left(1 + \left(\frac{r_{\text{ref}}}{r_{\text{mom}}}\right)^2 P_{20}(\cos\theta_{\text{mom}})C_{20}\right), \tag{5}$$

$$\begin{aligned}\underline{g}(\underline{r}) = {} & \frac{-GM}{r_{\text{mom}}^2}\left(1 + \frac{3}{2}\sqrt{5}\left(\frac{r_{\text{ref}}}{r_{\text{mom}}}\right)^2\right. \\ & \left.\times(3\cos^2\theta_{\text{mom}} - 1)C_{20}\right)\underline{\hat{r}_{\text{mom}}} \\ & - \frac{GM}{r_{\text{mom}}^2}\left(\frac{r_{\text{ref}}}{r_{\text{mom}}}\right)^2 \frac{1}{2}\sqrt{5}(6\cos\theta_{\text{mom}}\sin\theta_{\text{mom}}) \\ & \times C_{20}\underline{\hat{\theta}_{\text{mom}}}.\end{aligned} \tag{6}$$

Given the coefficients of the gravitational field and an initial position and velocity, the trajectory integration is straightforward. We describe it below to illustrate the techniques that will be used in the more complicated cases to follow.

Schematically, this trajectory reconstruction procedure can be expressed as

Begin with $t, x_{\text{inert}}, y_{\text{inert}}, z_{\text{inert}}, v_{x,\text{inert}}, v_{y,\text{inert}}, v_{z,\text{inert}}$.

Start loop:

$$x_{\text{inert}}, y_{\text{inert}}, z_{\text{inert}} \rightarrow r_{\text{mom}}, \theta_{\text{mom}}, \phi_{\text{mom}}, \tag{7a}$$

$$r_{\text{mom}}, \theta_{\text{mom}}, \phi_{\text{mom}} \rightarrow g_{r,\text{mom}}, g_{\theta,\text{mom}}, g_{\phi,\text{mom}}, \tag{7b}$$

$$g_{r,\text{mom}}, g_{\theta,\text{mom}}, g_{\phi,\text{mom}} \rightarrow g_{x.\text{inert}}, g_{y,\text{inert}}, g_{z,\text{inert}}, \tag{7c}$$

$$\mathrm{d}x_{\text{inert}} = v_{x,\text{inert}}\,\mathrm{d}t;\quad \mathrm{d}y_{\text{inert}} = v_{y,\text{inert}}\,\mathrm{d}t;$$

$$\mathrm{d}z_{\text{inert}} = v_{z,\text{inert}}\,\mathrm{d}t, \tag{7d}$$

$$\mathrm{d}v_{x,\text{inert}} = g_{x,\text{inert}}\,\mathrm{d}t;\quad \mathrm{d}v_{y,\text{inert}} = g_{y,\text{inert}}\,\mathrm{d}t;$$

$$\mathrm{d}v_{z,\text{inert}} = g_{z,\text{inert}}\,\mathrm{d}t, \tag{7e}$$

$$\text{Check if } r_{\text{inert}} < \textit{Planetary Radius}? \tag{7f}$$

Either stop or loop again.

The gravitational field is axisymmetric when truncated at second degree and order. In this case, gravitational accelerations in either of the inertial frames are functions of position only and can be found without needing to use the *momentary spherical* frame. If the gravitational field is not axisymmetric, then the gravitational effects of mass concentrations will rotate with the planet and gravitational accelerations in either of the inertial frames are functions of position and time. This technique, which is designed to be as general as possible, permits the use of non-axisymmetric gravitational fields. If only axisymmetric fields are to be considered, then the technique could be simplified.

To include aerodynamic accelerations, this procedure will be adapted to incorporate the transformation of aerodynamic acceleration from the frame of original measurements, which is fixed with respect to the spacecraft, to the *inertial Cartesian* frame.

3. The effects of an atmosphere on trajectory reconstructions

3.1. The spacecraft frame

Suppose that the accelerometer, which is rigidly mounted within the spacecraft, measures the linear accelerations of the spacecraft's centre of mass in three orthogonal directions. We define a fifth and final frame, called the *spacecraft frame,* consisting of right-handed Cartesian axes along these three orthogonal directions.

The axis most nearly parallel to the flow velocity during atmospheric entry is conventionally chosen as the z_{sct}-axis. For axisymmetric spacecraft, such as those with blunted cone shapes, this axis is also usually the axis of symmetry.

The orientation of the *spacecraft* frame, or spacecraft attitude, with respect to any of the other frames we have discussed so far is not fixed or necessarily known. The transformation of acceleration measurements between this frame and any of the other frames is the main complication to be addressed in this section of the paper. First we assume that an as-yet-undefined *attitude tracking function* exists that transforms the acceleration components $a_{\text{aero},x,\text{sct}}$, $a_{\text{aero},y,\text{sct}}$, $a_{\text{aero},z,\text{sct}}$ into the *inertial Cartesian* frame, $a_{\text{aero},x,\text{inert}}$, $a_{\text{aero},y,\text{inert}}$, $a_{\text{aero},z,\text{inert}}$. We then outline the solution procedure using this function. Finally, we discuss different ways of generating this *attitude tracking function* explicitly.

3.2. Addition of aerodynamics to the solution procedure

The trajectory reconstruction procedure from Section 2.5 is modified to include an additional calculation (Eq. (8e)) which transforms the linear accelerations of the spacecraft's centre of mass due to aerodynamic forces from the *spacecraft* frame to the *inertial Cartesian* frame, using the *attitude tracking function*, and to include these accelerations in the integration step.

Schematically, this trajectory reconstruction procedure can be expressed as:

Begin with $t, x_{\text{inert}}, y_{\text{inert}}, z_{\text{inert}}, v_{x,\text{inert}}, v_{y,\text{inert}}, v_{z,\text{inert}}$.

Start loop:

$$x_{\text{inert}}, y_{\text{inert}}, z_{\text{inert}} \rightarrow r_{\text{mom}}, \theta_{\text{mom}}, \phi_{\text{mom}}, \tag{8a}$$

$$r_{\text{mom}}, \theta_{\text{mom}}, \phi_{\text{mom}} \rightarrow g_{r,\text{mom}}, g_{\theta,\text{mom}}, g_{\phi,\text{mom}}, \tag{8b}$$

$$g_{r,\text{mom}}, g_{\theta,\text{mom}}, g_{\phi,\text{mom}} \rightarrow g_{x,\text{inert}}, g_{y,\text{inert}}, g_{z,\text{inert}}, \tag{8c}$$

$$\mathrm{d}x_{\mathrm{inert}} = v_{x,\mathrm{inert}}\,\mathrm{d}t;\quad \mathrm{d}y_{\mathrm{inert}} = v_{y,\mathrm{inert}}\,\mathrm{d}t;$$

$$\mathrm{d}z_{\mathrm{inert}} = v_{z,\mathrm{inert}}\,\mathrm{d}t, \tag{8d}$$

$$a_{\mathrm{aero},x,\mathrm{sct}}, a_{\mathrm{aero},y,\mathrm{sct}}, a_{\mathrm{aero},z,\mathrm{sct}} \rightarrow a_{\mathrm{aero},x,\mathrm{inert}}, a_{\mathrm{aero},y,\mathrm{inert}}, a_{\mathrm{aero},z,\mathrm{inert}}, \tag{8e}$$

$$\mathrm{d}v_{x,\mathrm{inert}} = (g_{x,\mathrm{inert}} + a_{\mathrm{aero},x,\mathrm{inert}})\,\mathrm{d}t;$$

$$\mathrm{d}v_{y,\mathrm{inert}} = (g_{y,\mathrm{inert}} + a_{\mathrm{aero},y,\mathrm{inert}})\,\mathrm{d}t;$$

$$\mathrm{d}v_{z,\mathrm{inert}} = (g_{z,\mathrm{inert}} + a_{\mathrm{aero},z,\mathrm{inert}})\,\mathrm{d}t, \tag{8f}$$

Check if $r_{\mathrm{inert}} < \textit{Planetary Radius}$? (8g)

Either stop or loop again.

The key to implementing the above approach successfully is constraining the attitude of the spacecraft. We discuss four options that can be used—*head-on*, *drag-only*, *acceleration ratios*, and *gyroscopes*. One of these four will be applicable to the vast majority of cases, but other options may exist.

3.3. The head-on option for constraining spacecraft attitude

This option assumes that the spacecraft aerodynamics and attitude during atmospheric entry are such that all aerodynamic forces acting on the spacecraft's centre of mass are directed along one of the axes, which we call the major axis, of the *spacecraft frame which is also* parallel to the flow velocity. The magnitude of the aerodynamic acceleration is assumed to be that of the major axis acceleration. Acceleration measurements along the other two minor axes are ignored, regardless of their importance. The direction of the aerodynamic acceleration is assumed to be parallel to the known flow velocity. This is considered reasonable since spacecraft with a blunted cone shape are usually approximately axisymmetric, with the axis of symmetry being roughly parallel to both the flow velocity and the major *spacecraft frame* axis, conventionally the z-axis. Galileo used this option (Seiff et al., 1998). In neglecting acceleration measurements from the two other minor axes, we assume that they contain nothing but noise, which is a source of error. Since the spacecraft is unlikely to align itself precisely along the flow velocity at all times, the direction in which the acceleration is assumed to act will not be precisely correct and this is another source of error. The flow velocity is the relative velocity of the fluid with respect to the spacecraft in an inertial frame. The atmosphere is assumed to rotate with the same angular velocity as the planet.

The *attitude-tracking* step of the trajectory reconstruction for the *head-on* option can be expressed schematically as

$$\underline{v}_{\mathrm{wind,inert}} = \omega\widehat{\underline{z}}_{\mathrm{inert}} \times \underline{r}, \tag{9a}$$

$$\underline{v}_{\mathrm{rel,inert}} = \underline{v}_{\mathrm{inert}} - \underline{v}_{\mathrm{wind,inert}}, \tag{9b}$$

$$|\underline{v}_{\mathrm{rel}}| = \sqrt{(v^2_{\mathrm{rel},x,\mathrm{inert}} + v^2_{\mathrm{rel},y,\mathrm{inert}} + v^2_{\mathrm{rel},z,\mathrm{inert}})}, \tag{9c}$$

$$|\underline{a}_{\mathrm{aero}}| = \sqrt{(a^2_{\mathrm{aero},z,\mathrm{sct}})}, \tag{9d}$$

$$\underline{a}_{\mathrm{aero,inert}} = -1 \times \frac{|a_{\mathrm{aero}}|}{|\underline{v}_{\mathrm{rel}}|}\underline{v}_{\mathrm{rel,inert}}. \tag{9e}$$

3.4. The drag-only option for constraining spacecraft attitude

This option assumes that the spacecraft aerodynamics and attitude during atmospheric entry are such that all aerodynamic forces acting on the spacecraft's centre of mass are directed parallel to the flow velocity, but that this is not necessarily parallel to the major axis of the spacecraft. The square root of the sum of squares of the three orthogonal acceleration measurements in the *spacecraft frame* is the magnitude of the total aerodynamic acceleration. This option assumes that there are no aerodynamic forces, called lift forces or side forces, acting orthogonal to the flow velocity. If the two minor axis acceleration measurements are predominantly due to noise and rotational effects, then it is not useful to use them to reconstruct the spacecraft's trajectory and the *head-on* option is better than the *drag-only* option. If, on the other hand, the spacecraft is usually several degrees away from being head-on to the flow, then these two minor axis acceleration measurements will be sensitive to those components of the aerodynamic acceleration along the flow vector that are not parallel to the major axis of the spacecraft frame. In this case, the *drag-only* option is better than the *head-on* option because it includes these accelerations in the trajectory reconstruction. The *drag-only* option works well if the spacecraft aerodynamics are designed to minimise aerodynamic forces perpendicular to the flow velocity. One example of a class of objects which works well with this option is a sphere. Aeroplanes, which use their wings to generate lift, would be very badly modelled with this approach.

The *attitude tracking* step of the trajectory reconstruction for the *drag-only* option can be expressed schematically as

$$\underline{v}_{\mathrm{wind,inert}} = \omega\widehat{\underline{z}}_{\mathrm{inert}} \times \underline{r}, \tag{10a}$$

$$\underline{v}_{\mathrm{rel,inert}} = \underline{v}_{\mathrm{inert}} - \underline{v}_{\mathrm{wind,inert}}, \tag{10b}$$

$$|\underline{v}_{\mathrm{rel}}| = \sqrt{(v^2_{\mathrm{rel},x,\mathrm{inert}} + v^2_{\mathrm{rel},y,\mathrm{inert}} + v^2_{\mathrm{rel},z,\mathrm{inert}})}, \tag{10c}$$

$$|\underline{a}_{\mathrm{aero}}| = \sqrt{(a^2_{\mathrm{aero},x,\mathrm{sct}} + a^2_{\mathrm{aero},y,\mathrm{sct}} + a^2_{\mathrm{aero},z,\mathrm{sct}})}, \tag{10d}$$

$$\underline{a}_{\mathrm{aero,inert}} = -1 \times \frac{|a_{\mathrm{aero}}|}{|\underline{v}_{\mathrm{rel}}|}\underline{v}_{\mathrm{rel,inert}}. \tag{10e}$$

3.5. The acceleration ratios option for constraining spacecraft attitude

If the aerodynamic properties of the spacecraft are well-constrained and not a singular case, then the ratio of

linear accelerations along any pair of *spacecraft frame* axes uniquely defines one of the two angles necessary to define the spacecraft attitude with respect to the flow velocity (Peterson, 1965a). Forming a second ratio of linear accelerations along a different pair of *spacecraft frame* axes uniquely defines the second and final angle. PAET used this option (Seiff et al., 1973). As in the *drag-only* option, the square root of the sum of squares of the three orthogonal acceleration measurements in the *spacecraft frame* is the magnitude of the total aerodynamic acceleration. Unlike the *drag-only* option, the direction of the aerodynamic acceleration is known since the spacecraft attitude is known, rather than it being assumed to be parallel to the flow velocity.

The *acceleration ratios* option offers an unexpectedly elegant way to constrain spacecraft attitude indirectly (Peterson, 1965a). For a known fluid composition and thermodynamic state, an axisymmetric spacecraft of known mass, size, and shape, and a known fluid speed with respect to the spacecraft, only the angle between the spacecraft symmetry axis and the flow direction is needed to constrain completely the forces acting parallel to and perpendicular to the symmetry axis of the spacecraft. The thermodynamic state is defined by pressure and temperature or any other pair of intensive thermodynamic variables. Numerical modelling and wind-tunnel experiments can generate an expression for the parallel force as a function of this angle and a similar expression for the perpendicular force. The ratio of these two forces, equal to the measurable ratio of accelerations, can also be expressed as a function of this angle. If this function is single-valued, then it can be inverted into an expression for spacecraft attitude angle as a function of acceleration ratio. Thus, the ratio of linear accelerations measured in the spacecraft frame can uniquely define the attitude of the spacecraft. Extension to asymmetric spacecraft is simple, involving the $a_{\mathrm{aero},x,\mathrm{sct}}/a_{\mathrm{aero},z,\mathrm{sct}}$ and $a_{\mathrm{aero},y,\mathrm{sct}}/a_{\mathrm{aero},z,\mathrm{sct}}$ acceleration ratios constraining the two angles necessary to define spacecraft attitude relative to the velocity vector of the fluid. Note that only two angles, rather than the traditional three Euler angles, are required to completely define the orientation of the *spacecraft* frame relative to the *inertial Cartesian* frame since a third piece of directional information is supplied by the velocity vector of the fluid. The details of the transformation from the *spacecraft* frame to the *inertial Cartesian* frame depend on the definition of the two angles, α and β, and may be worked out using a text on the motions of a rigid body and relevant co-ordinate transformations, such as Goldstein (1980).

The requirement for the acceleration ratios to be "well-behaved" functions of spacecraft attitude is usually satisfied. However, the *acceleration ratios* option requires knowledge of the atmospheric density, pressure, and temperature as the trajectory reconstruction is being carried out, whereas the other options separate the trajectory and atmospheric structure reconstruction processes completely. This option also requires a comprehensive knowledge of the spacecraft aerodynamics as a function of atmospheric pressure and temperature and spacecraft speed and attitude. The other options do not require this information until the atmospheric structure reconstruction.

In some cases, the x, y, and z axis accelerations and the spacecraft aerodynamics might not all be known accurately enough to provide very useful constraints on spacecraft attitude. A simpler option, such as the *head-on* or *drag-only* options, might be all that is justified.

The aerodynamic database needed for the *acceleration ratios* option must contain the values of the $a_{\mathrm{aero},x,\mathrm{sct}}/a_{\mathrm{aero},z,\mathrm{sct}}$ and $a_{\mathrm{aero},y,\mathrm{sct}}/a_{\mathrm{aero},z,\mathrm{sct}}$ acceleration ratios for all possible values of fluid composition, pressure, temperature, speed with respect to the spacecraft, and the two angles, α, β, necessary to define spacecraft attitude. α and β must be clearly defined relative to the orientation of the velocity vector in the *spacecraft frame* and Peterson (1965a) offers one convention.

Since the aerodynamic properties of the spacecraft vary with atmospheric pressure and temperature, assumed profiles of atmospheric pressure and temperature must be used in the trajectory reconstruction. After the trajectory reconstruction is completed, profiles of atmospheric pressure and temperature will be derived using the reconstructed trajectory. If these profiles derived using the results of the trajectory reconstruction are not the same as the assumed profiles that went into the trajectory reconstruction, then the process is inconsistent. The trajectory reconstruction should be repeated using these derived profiles and then the atmospheric structure reconstruction should be repeated using the updated trajectory. This process should be iterated until the assumed profiles used in the trajectory reconstruction match the profiles derived from the subsequent atmospheric structure reconstruction. Only a small number of iterations is usually needed (Magalhães et al., 1999). This iteration can only be done after the entry is complete; so it cannot be used during the entry to control the spacecraft.

The *attitude tracking* step of the trajectory reconstruction for the *acceleration ratios* option can be expressed schematically as

$$\underline{v}_{\mathrm{wind,inert}} = \omega \underline{\hat{z}}_{\mathrm{inert}} \times \underline{r}, \tag{11a}$$

$$\underline{v}_{\mathrm{rel,inert}} = \underline{v}_{\mathrm{inert}} - \underline{v}_{\mathrm{wind,inert}}, \tag{11b}$$

$$\textit{composition}, p, T, |\underline{v}_{\mathrm{rel}}| \rightarrow \frac{a_{\mathrm{aero},x,\mathrm{sct}}}{a_{\mathrm{aero},z,\mathrm{sct}}}(\alpha,\beta), \frac{a_{\mathrm{aero},y,\mathrm{sct}}}{a_{\mathrm{aero},z,\mathrm{sct}}}(\alpha,\beta), \tag{11c}$$

$$\frac{a_{\mathrm{aero},x,\mathrm{sct}}}{a_{\mathrm{aero},z,\mathrm{sct}}}(\alpha,\beta), \quad \frac{a_{\mathrm{aero},y,\mathrm{sct}}}{a_{\mathrm{aero},z,\mathrm{sct}}}(\alpha,\beta) \rightarrow \alpha\left(\frac{a_{\mathrm{aero},x,\mathrm{sct}}}{a_{\mathrm{aero},z,\mathrm{sct}}}, \frac{a_{\mathrm{aero},y,\mathrm{sct}}}{a_{\mathrm{aero},z,\mathrm{sct}}}\right), \beta\left(\frac{a_{\mathrm{aero},x,\mathrm{sct}}}{a_{\mathrm{aero},z,\mathrm{sct}}}, \frac{a_{\mathrm{aero},y,\mathrm{sct}}}{a_{\mathrm{aero},z,\mathrm{sct}}}\right), \tag{11d}$$

$$\alpha, \beta, \underline{v}_{\mathrm{rel,inert}}, \underline{a}_{\mathrm{aero,sct}} \rightarrow \underline{a}_{\mathrm{aero,inert}}. \tag{11e}$$

3.6. The gyroscopes option for constraining spacecraft attitude

Gyroscopes measure the angular acceleration of the *spacecraft frame* about its centre of mass. These additional measurements are incorporated into the equations of motion for a rigid body, which then yield spacecraft position, velocity, attitude, and angular velocity all along the trajectory. An initial angular position and velocity, possibly provided by star tracking, are required as initial conditions. Viking used this option (Seiff and Kirk, 1977). As in the *acceleration ratios* option, the square root of the sum of the squares of the three orthogonal acceleration measurements in the *spacecraft frame* is the magnitude of the total aerodynamic acceleration. Unlike the *acceleration ratios* option, spacecraft attitude, which gives the direction of the aerodynamic acceleration in a useful frame, is tracked directly, rather than being inferred from measured acceleration ratios and an aerodynamic database. The *gyroscopes* option is, in principle, the best of the four. However, the additional instruments required by this option need money, mass, and volume that might not be available. For spacecraft that satisfy any of the first three options, gyroscopes are a redundant luxury for trajectory and atmospheric structure reconstruction. However, operational requirements to monitor the engineering performance of the spacecraft might justify that redundancy.

This approach is more complicated than simply inserting a subroutine into the pre-existing algorithm; so we will outline the entire algorithm. The relationship between the *spacecraft* frame and the *inertial Cartesian* frame can be described using Euler angles. These three angles provide sufficient information to transform acceleration measurements made in the *spacecraft* frame into the *inertial Cartesian* frame. There are many arbitrary conventions concerning Euler angles. Here we use the *xyz*-convention of Goldstein (1980, p. 608), in which Goldstein's unprimed co-ordinate system is the *inertial Cartesian* frame and Goldstein's primed co-ordinate system is the *spacecraft* frame. This choice allows rates of change of the Euler angles to be expressed in terms of the Euler angles and angular velocities in the *spacecraft* frame, which simplifies the integration. In actual calculations, quaternions may be preferred because Euler angles can be indeterminate for certain attitudes—just as the east longitude of the north pole is indeterminate. We present Euler angles here because the formulation is relatively simple.

The Euler matrix in the *xyz*-convention, $\underline{\underline{EM}}$, is constructed from the Euler angles as described in Goldstein (1980) and enables the conversion of vectors between the *inertial Cartesian* (unprimed) frame and the *spacecraft* (primed) frame

$$\underline{x'} = \underline{\underline{EM}}\ \underline{x}. \tag{12}$$

We expand the initial condition to include the three Euler angles and the angular velocity of the spacecraft about its axes at the appropriate time. For example, the angular velocity might be a predetermined spin. The Euler angles change with time due to the rotation of the spacecraft about its axes. Rearrangement of Goldstein's equations B-14*xyz* (1980, p. 609) gives

$$\dot{\phi}_{\text{Euler}} = \frac{\Omega_{y,\text{sct}} \sin\psi_{\text{Euler}} + \Omega_{z,\text{sct}} \cos\psi_{\text{Euler}}}{\cos\theta_{\text{Euler}}}, \tag{13a}$$

$$\dot{\psi}_{\text{Euler}} = \Omega_{x,\text{sct}} + \tan\theta_{\text{Euler}} \times (\Omega_{y,\text{sct}} \sin\psi_{\text{Euler}} + \Omega_{z,\text{sct}} \cos\psi_{\text{Euler}}), \tag{13b}$$

$$\dot{\theta}_{\text{Euler}} = \Omega_{y,\text{sct}} \cos\psi_{\text{Euler}} - \Omega_{z,\text{sct}} \sin\psi_{\text{Euler}}. \tag{13c}$$

$\dot{\Omega}_{x,\text{sct}}$, $\dot{\Omega}_{y,\text{sct}}$, $\dot{\Omega}_{z,\text{sct}}$ are the three components of the angular acceleration of the spacecraft about the three *spacecraft* frame axes. They are directly measured by the gyroscopes.

The full trajectory reconstruction for the *gyroscopes* option can be expressed schematically as

Begin with t, x_{inert}, y_{inert}, z_{inert}, $v_{x,\text{inert}}$, $v_{y,\text{inert}}$, $v_{z,\text{inert}}$, φ_{Euler}, ψ_{Euler}, θ_{Euler}, $\dot{\Omega}_{x,\text{sct}}$, $\dot{\Omega}_{y,\text{sct}}$, $\dot{\Omega}_{z,\text{sct}}$.

Start loop:

$$x_{\text{inert}},\ y_{\text{inert}},\ z_{\text{inert}} \rightarrow r_{\text{mom}},\ \theta_{\text{mom}},\ \phi_{\text{mom}}, \tag{14a}$$

$$r_{\text{mom}},\ \theta_{\text{mom}},\ \phi_{\text{mom}} \rightarrow g_{r,\text{mom}},\ g_{\theta,\text{mom}},\ g_{\phi,\text{mom}}, \tag{14b}$$

$$g_{r,\text{mom}},\ g_{\theta,\text{mom}},\ g_{\phi,\text{mom}} \rightarrow g_{x.\text{inert}},\ g_{y,\text{inert}},\ g_{z,\text{inert}}, \tag{14c}$$

$$\phi_{\text{Euler}},\ \psi_{\text{Euler}},\ \theta_{\text{Euler}} \rightarrow \underline{\underline{EM}}, \tag{14d}$$

$$\underline{a_{\text{aero,inert}}} = \underline{\underline{EM}}\ \underline{a_{\text{aero,sct}}}, \tag{14e}$$

$$\mathrm{d}x_{\text{inert}} = v_{x,\text{inert}}\,\mathrm{d}t;\quad \mathrm{d}y_{\text{inert}} = v_{y,\text{inert}}\,\mathrm{d}t;\quad \mathrm{d}z_{\text{inert}} = v_{z,\text{inert}}\,\mathrm{d}t, \tag{14f}$$

$$\mathrm{d}v_{x,\text{inert}} = (g_{x,\text{inert}} + a_{\text{aero},x,\text{inert}})\,\mathrm{d}t;$$
$$\mathrm{d}v_{y,\text{inert}} = (g_{y,\text{inert}} + a_{\text{aero},y,\text{inert}})\,\mathrm{d}t;$$
$$\mathrm{d}v_{z,\text{inert}} = (g_{z,\text{inert}} + a_{\text{aero},z,\text{inert}})\,\mathrm{d}t, \tag{14g}$$

$$\mathrm{d}\phi = \left(\frac{\Omega_{y,\text{sct}} \sin\psi + \Omega_{z,\text{sct}} \cos\psi}{\cos\theta}\right)\mathrm{d}t, \tag{14h}$$

$$\mathrm{d}\psi = (\Omega_{x,\text{sct}} + \tan\theta \times (\Omega_{y,\text{sct}} \sin\psi + \Omega_{z,\text{sct}} \cos\psi))\,\mathrm{d}t, \tag{14i}$$

$$\mathrm{d}\theta = (\Omega_{y,\text{sct}} \cos\psi - \Omega_{z,\text{sct}} \sin\psi)\,\mathrm{d}t, \tag{14j}$$

$$\mathrm{d}\Omega_{x,\text{sct}} = \dot{\Omega}_{x,\text{sct}}\,\mathrm{d}t;\quad \mathrm{d}\Omega_{y,\text{sct}} = \dot{\Omega}_{y,\text{sct}}\,\mathrm{d}t;$$
$$\mathrm{d}\Omega_{z,\text{sct}} = \dot{\Omega}_{z,\text{sct}}\,\mathrm{d}t, \tag{14k}$$

$$\text{Check if } r_{\text{inert}} < \textit{Planetary Radius}? \tag{14l}$$

Either stop or loop again.

3.7. Summary of techniques used to constrain spacecraft attitude

The *head-on*, *drag-only*, and *acceleration ratios* options require knowledge of the flow velocity. The simplest assumption is that the atmosphere of the planet is rotating with the same angular velocity as the interior of the planet. Atmospheric bulk motions, winds, can modify this flow pattern. If precise knowledge of the flow velocity is important, then direct wind measurements or predictions from climate models can be used to define it.

The *head-on* and *drag-only* options are simple to implement and do not require any additional datasets such as aerodynamic databases or in-flight gyroscopic measurements, but use idealised, approximate aerodynamics that introduce uncertainties. The *acceleration ratios* option can indirectly reconstruct spacecraft attitude without any additional flight hardware, but requires an accurate aerodynamic database and may accumulate uncertainties during the indirect reconstruction process. The *gyroscopes* option can directly reconstruct spacecraft attitude, but requires additional flight hardware. Unless the spacecraft has a significant amount of lift, the simple *head-on* or *drag-only* options often give just as useful results for the trajectory and atmospheric structure reconstruction as the more complicated and expensive *acceleration ratios* or *gyroscopes* options.

3.8. Parachute considerations

Many planetary entry spacecraft deploy parachutes. These would be torn apart if deployed early in the entry when the spacecraft is typically travelling at hypersonic speeds. Deployed at slower, near-sonic speeds, they decrease the terminal velocity of descent and allow the spacecraft to make more scientific measurements during descent. They also allow landings without large retrorockets. The aerodynamic properties of disk-gap-band parachutes, a common type for planetary spacecraft, are much more complicated than those of the aeroshells which typically encase spacecraft during entry (Bendura et al., 1974; Braun et al., 1999). This makes the *acceleration ratios* option impractical after parachute deployment. Apart from that, the main effect of parachute deployment on the trajectory reconstruction is to introduce some oscillatory motions into the spacecraft, and hence into the measured accelerations as well, as it swings around on the end of its parachute (Magalhães et al., 1999). Trajectory reconstructions using the *head-on* or *drag-only* options will be correct in an average sense, but the actual trajectory will deviate from this reconstruction due to the swinging of the spacecraft. Trajectory reconstructions using the *gyroscopes* option should remain accurate. In practice, the sampling rate is often reduced after parachute deployment to reduce data volume and care must obviously be taken that this does not degrade the reconstruction.

3.9. Error considerations

Several sources of error, such as winds, have been mentioned thus far. There are many others, including uncertainties in the spacecraft's entry state, in the planet's gravitational field, in the end-to-end gain and offset of the accelerometers and their temperature dependences, in the alignment and position of the accelerometers, and also noise, numerical accuracy of reconstruction software, and the digitization of the accelerometer signal (Peterson, 1965b). The effects of these errors and uncertainties on the accuracy of the trajectory reconstruction can be estimated as follows (Peterson, 1965b):

The spacing in time of points along the reconstructed trajectory is controlled by the accelerometer sampling rate. For example, 10 Hz sampling gives a spacing of 0.1 s.

The vertical resolution of the data points is the ratio of the vertical speed and the accelerometer sampling rate. For example, a vertical speed at entry of 1 km s^{-1} and a sampling rate of 10 Hz corresponds to a vertical resolution of 100 m.

The uncertainty in the absolute altitude of each data point will be affected by:

- Acceleration uncertainty and error, Δa, due to instrument resolution, noise, changes in gain and offset since calibration, any systematic offset, corrections for off-centre instrument position, etc., integrates to an uncertainty in altitude of $0.5t^2 \times \Delta a$. For example, Δa of 10^{-4} m s^{-2} and t of 1000 s gives an uncertainty of 50 m.
- Uncertainty in the gravitational field, Δg, at a known position integrates to an uncertainty in altitude of $0.5t^2 \times \Delta g$. For example, Δg of 10^{-4} m s^{-2} and t of 1000 s gives an uncertainty of 50 m.
- Uncertainty in vertical entry velocity, Δv, integrates to an uncertainty in altitude of $t \times \Delta v$. For example, Δv of 0.1 m s^{-1} and t of 1000 s gives an uncertainty of 100 m.
- Uncertainty in the entry state altitude, which was about 2 km for Pathfinder (Magalhães et al., 1999). If the planet's topography is well known, then the landed altitude may be known to better than this from the landed latitude and east longitude, although this requires integrating backwards in time through the parachute region of descent. Uncertainties in landed latitude and east longitude may still be large, but selection of a relatively flat target for landing ensures a relatively small uncertainty in altitude. This landed position can be used in preference to the entry position as a boundary condition on the integration for the trajectory reconstruction. For example, 100 m may be the uncertainty in altitude for a landing on flat terrain with much larger uncertainties in horizontal position.
- Uncertainty in gravitational acceleration due to uncertainty in position. Uncertainty in gravity equals uncertainty in altitude $\times 2g/r$. This is in addition to any uncertainties in the gravitational field at any known position. This should be included with the earlier Δg term.

The uncertainties in the absolute latitude and east longitude of each data point will be affected by

- Acceleration uncertainty and error, Δa, as discussed above with reference to altitude.
- Uncertainty in horizontal entry velocity, Δv, yields an uncertainty in altitude of $t \times \Delta v$. For example, Δv of 0.1 m s^{-1} and t of 1000 s gives an uncertainty of 100 m.
- Uncertainty in the entry state latitude and east longitude, which was about 2 km for Pathfinder (Magalhães et al., 1999).

Since the errors in position due to acceleration uncertainties and errors accumulate as the square of time since entry, it is imperative that the accelerometers be well calibrated. Whilst the error due to noise is important on short timescales, but averages to zero on long timescales, any offset or gain error will be cumulative through the integration process.

In practice, accelerometers are rarely mounted at the spacecraft's exact centre of mass. In addition to aerodynamic accelerations, these poorly positioned accelerometers will also measure terms due to the angular motions of the spacecraft about its centre of mass. If these are periodic, they can be isolated within the measured accelerations and removed. The justification for this additional data processing is strongest if the period can be related to known properties of the spacecraft, such as its moments of inertia. For example, Spencer et al. (1999) identified a signal related to the 2-rpm roll rate of Pathfinder in its accelerometer measurements. However, unless there is a justification for the periodic acceleration, it is not known whether or not it is appropriate to remove it, as it might be signal, not noise. If the x- and y-axis aerodynamic accelerations are small, due to the majority of the aerodynamic accelerations being aligned with the z-axis, and the x- and y-axis accelerometers are located far enough from the centre of mass to have their measurements significantly affected by these rotational terms, then it may be best to neglect the x- and y-axis measurements and just use the z-axis measurements in the *head-on* option.

Whichever option is used for constraining spacecraft attitude, the transformation of measured accelerations from the *spacecraft* frame to the *inertial Cartesian* frame introduces additional uncertainties. The uncertainties introduced by the *head-on* and *drag-only* options should be estimated by, e.g., altering the prescribed direction of the acceleration vector by some amount and performing another trajectory reconstruction with this altered dataset. Maximum likely changes in direction will have to be estimated from the aerodynamic modelling work that was used to justify the use of these simple options. Comparison to the nominal trajectory reconstruction will provide an estimate of the uncertainties that could accumulate under these options. The uncertainties introduced by the *acceleration ratios* option should be found by formally propagating the uncertainties in the measured accelerations and in the aerodynamic database through the various steps in the frame transformation procedure. The uncertainties introduced by the *gyroscopes* option should be calculated by propagating the additional instrumental and entry state uncertainties through the frame transformation procedure. The *head-on*, *drag-only*, and *acceleration ratios* options should compare likely atmospheric winds beyond those included in the trajectory reconstruction to the spacecraft velocity and propagate this uncertainty in the velocity of the spacecraft relative to the atmosphere through the various steps in the frame transformation procedure.

Generally mission goals, such as accuracy of reconstructed position and velocity, are set before flight and a detailed uncertainty analysis can evaluate if the proposed instrument specifications can achieve those goals. Since space missions involve redundancy, further constraints on the trajectory reconstruction, which reduce the errors, can be provided by additional information such as:

- The Doppler shift of telemetry during descent places crude constraints on the descent speed. The transmitted frequency of the telemetry is not usually known well enough to provide very accurate constraints.
- Any radar altimetry during descent, which is nominally a trigger for events during entry, descent, and landing, constrains the altitude and descent speed if the underlying topography is "well-behaved" or known.
- The Doppler shift of transmissions after landing enables the landing site position to be located to very high precision and accuracy. This will be most helpful if the spacecraft does not roll/bounce too far between its initial impact and coming to rest.
- The measured acceleration due to gravity at the landing site places crude constraints on the accuracy of the accelerometers. Uncertainties in the gravitational field at the landing site mean that this does not provide very accurate constraints. The landed orientation of the spacecraft will be known from images of its surroundings, so any tilt can be corrected for.

4. Trajectory reconstruction applied to Mars Pathfinder

4.1. Technical details

We have written computer programmes in Research Systems's IDL programming language, which perform a trajectory reconstruction as discussed in the previous section. The *head-on*, *drag-only*, and *gyroscopes* options have been implemented. At the time we developed these programmes, we did not have access to a realistic aerodynamic database for a planetary entry spacecraft; so we have not yet implemented the *acceleration ratios* option. We have recently been made aware of the publication of a significant portion of the Pathfinder aerodynamic database in Moss et al. (1998) and Gnoffo et al. (1996). We hope to use this database to implement the *acceleration ratios*

option in our programmes in the future. The integration is performed using IDL's fourth order Runge-Kutta procedure when accuracy is most important. We have tested it on the publicly available Mars Pathfinder dataset, PDS volume MPAM_0001 (Golombek et al., 1997; Golombek, 1999). All the information necessary to reconstruct Pathfinder's trajectory is present in this volume. The dataset is online at http://atmos.nmsu.edu/PDS/data/mpam_0001/.

Since Pathfinder was not equipped with gyroscopes, our trajectory reconstruction is restricted to using the *head-on* or *drag-only* options for determining spacecraft attitude. Since work by the Pathfinder accelerometer engineering and science teams using a good aerodynamic database and the *acceleration ratios* option showed that Pathfinder's symmetry axis is very close to the direction of aerodynamic decelerations experienced during its atmospheric entry, we were able to use the *head-on* option in our trajectory reconstruction (Spencer et al., 1999; Magalhães et al., 1999).

4.2. Assembly and preparation of Pathfinder's accelerometer data

Pathfinder's entry state, as stated in the PDS file /document/edlddrds.htm, is a radial distance from the centre of mass of Mars, r, of 3597.2 ± 1.7 km, an areocentric latitude, θ, of $23 \pm 0.04°$N, an east longitude, ϕ, of $343.67 \pm 0.01°$E, an entry speed, v_{entry}, of 7444.7 ± 0.7 m s^{-1}, a flight path angle below the horizontal, γ, of $16.85 \pm 0.02°$, and a flight path azimuth measured clockwise from north, ψ, of $255.41 \pm 0.02°$. All these are quoted in a Mars-fixed, i.e., rotating, co-ordinate system on July 4, 1997, 1651:12.28 UTC. We refer to this entry state as the PDS entry state.

The spacecraft position in this frame is identical to position in the *momentary spherical* frame at this instant; so it can easily be transformed into the *inertial Cartesian* frame for the first step in the trajectory integration using the results of Section 2.4. The spacecraft velocity can be transformed from this frame into the *inertial spherical* frame as follows:

$$v_{r,\text{mom}} = -v_{\text{entry}} \sin\gamma, \tag{15a}$$

$$v_{\theta,\text{mom}} = -v_{\text{entry}} \cos\gamma \cos\psi, \tag{15b}$$

$$v_{\phi,\text{mom}} = v_{\text{entry}} \cos\gamma \sin\psi + \omega r \sin\theta. \tag{15c}$$

An alternative entry state has been published by the Pathfinder engineers (Spencer et al., 1999). In theory, a trajectory reconstruction using one entry state should pass through the other entry state. This entry state, which we label as the engineering entry state, is a radial distance from the centre of mass of Mars, r, of 3522 km, an aerocentric latitude, θ, of 22.6303°N, an east longitude, ϕ, of 337.9976°E, an entry speed, v_{entry}, of 7264.2 m s^{-1}, a flight path angle below the horizontal, γ, of 14.0614°, and a flight path azimuth measured clockwise from north, ψ, of 253.1481°. The relevant time is July 4, 1997, 1651:50.482 UTC. Uncertainties were not published. The position is once again quoted in the Mars-fixed, i.e., rotating, co-ordinate system, but the velocity is not. The velocity is given in an inertial, i.e., non-rotating, co-ordinate system. The spacecraft velocity can be transformed from this frame into the *inertial spherical* frame as follows:

$$v_{r,\text{mom}} = -v_{\text{entry}} \sin\gamma, \tag{16a}$$

$$v_{\theta,\text{mom}} = -v_{\text{entry}} \cos\gamma \cos\psi, \tag{16b}$$

$$v_{\phi,\text{mom}} = v_{\text{entry}} \cos\gamma \sin\psi \tag{16c}$$

Note that Eq. (16) is identical to Eq. (15) with $\omega = 0$. The PDS entry state corresponds to an altitude of about 210 km above the final landing site; the engineering entry state, about 38 s later, corresponds to an altitude of about 130 km. We shall initially use the PDS entry state.

There are many files of accelerometer data archived in the PDS volume in the /edl_erdr directory. As discussed in the file /document/edler_ds.htm, the best is the file /edl_erdr/r_sacc_s.tab because of its high (32 Hz) sampling rate. The data need to be multiplied by a reference value for the Earth's gravity, 9.795433 m s^{-2}, which is given in the file /edl_erdr/r_sacc_s.lbl.

One x-axis data point is 0.0, a clear outlier from the neighbouring data points. One z-axis data point is also 0.0 and an outlier. These are mentioned in Magalhães et al. (1999) but not in the file /document/edler_ds.htm. We replaced these with an interpolation from neighbouring data points. There are also about 10 data points in the y-axis data that are zero. However, these are consistent with neighbouring data points and have not been modified.

The accelerometers have several different gain states. The gain state of each accelerometer changed several times during atmospheric entry. When an accelerometer changes gain state, there is a brief acceleration pulse that is an artefact of the electronic time constant of the sensor (Magalhães et al., 1999). From calibration studies, as discussed in the file /document/edlddrds.htm, it was found that 1 s worth of data is corrupted immediately after a change in gain state. Gain state changes can be located by examining the listing of the gain states of each accelerometer as a function of time in the file /edl_erdr/r_sacc_s.lbl. The corrupted 1 s intervals of data were replaced with an interpolation from neighbouring data points.

The accelerometers continued to record data for a short time after impact when the spacecraft was bouncing and rolling around on the surface. The *head-on* option for constraining spacecraft attitude is clearly useless after impact; so all data recorded after landing are discarded from the data files. The moment of impact is easily identified in the accelerometer data as the first of a series of 10 g spikes in the accelerometer data, each about half a second in duration.

The first acceleration measurements are made at 1 Hz, not 32 Hz. For computational simplicity, we interpolated the earliest measurements to the same sampling rate as the rest of the dataset.

Acceleration measurements in the data file begin earlier than the PDS entry state. Those that precede the initial position and velocity that provide the boundary conditions for the trajectory integration are discarded, although of course they could be back integrated to recover the trajectory prior to the entry state. The files /edl_erdr/r_sacc_s.lbl and /edl_erdr/r_sacc_s.tab provide the times of each data point.

The planetary sidereal day of 24.6229 h is necessary for all the frame transformations (Lodders and Fegley, 1998). The planet's gravitational field is specified by GM, r_{ref}, and C_{20}, as discussed in Section 2.5. These values are updated regularly in light of improved data, but significant changes are confined to the higher order terms. The original reconstructions of the Mars Pathfinder trajectory and atmospheric structure occurred before the MGS revolution in martian geodesy and used values from the model GMM-1 (Smith et al., 1993).

The relevant values are:

$$GM = 4.282828 \times 10^{13}\ \mathrm{m^3\,s^{-2}}, \tag{17a}$$

$$r_{\mathrm{ref}} = 3394.2\ \mathrm{km}, \tag{17b}$$

$$C_{20} = -8.75977 \times 10^{-4}. \tag{17c}$$

This value for C_{20} corresponds to a normalisation convention for P_{20} of $P_{20}(1) = \sqrt{5}$ (Kaula, 1966).

Since our aim is to reproduce the archived Pathfinder results, we did not use the latest values for these parameters. Higher order terms are neglected since they are not large enough to significantly affect the trajectory reconstruction.

This is all the information necessary to reconstruct the trajectory of Mars Pathfinder. For convenience, we also tracked the altitude of the reconstructed trajectory above the landing site by subtracting the planetary radius of the final landing site, 3389.715 km, from the reconstructed radial distances. This is given in the file /document/edlddrds.htm to six significant figures and in Magalhães et al. (1999). All references to "altitude" imply radial distance with this value subtracted—never distance from an equipotential or any other reference surface.

To verify our trajectory reconstruction, we compared it to that archived with the PDS in files /edl_ddr/edl_ddr.lbl and /edl_ddr/edl_ddr.tab. This archived trajectory begins at an altitude of about 140 km, significantly below the PDS entry state at 210 km altitude. It ends at parachute deployment, at about 10 km altitude.

4.3. Entry state problems

Using the PDS entry state at 210 km, our reconstructed trajectory systematically differs from the PDS's by about a degree in both latitude and east longitude, as shown in Figs 1 and 2. Our latitudes as a function of time are about a degree south of the PDS's. Our east longitudes as a function of time are about a degree east of the PDS's. These

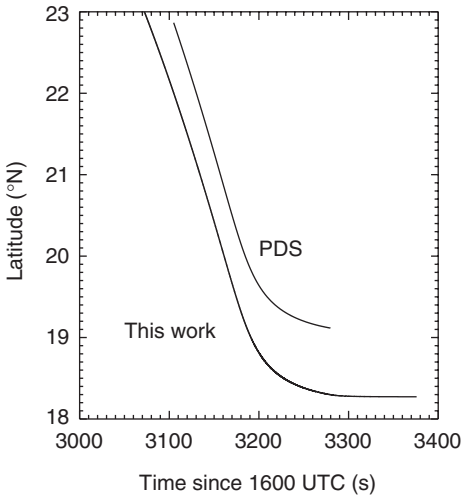

Fig. 1. Reconstructed latitude as a function of time from the PDS archive and the results of this paper using the PDS entry state. The PDS trajectory extends from 140 to 10 km altitude. The trajectory derived in this paper extends from 210 to 0 km altitude.

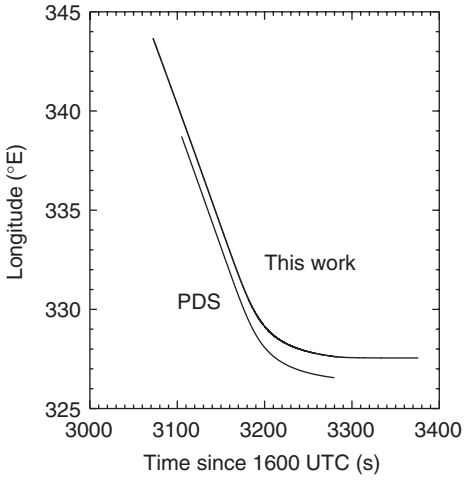

Fig. 2. As in Fig. 1, but east longitude.

are many times greater than the hundredths of degree-scale uncertainties in latitude and east longitude in the PDS entry state. A significant problem exists in either our work or the PDS archive. The trajectory archived with the PDS only extends up to 140 km altitude, yet Fig. 2 of Magalhães et al. (1999) shows the trajectory up to 210 km altitude. Below 140 km altitude, the PDS trajectory and Fig. 2 of Magalhães et al. appear identical under visual inspection. Magalhães et al. quote the PDS entry state exactly as the initial conditions used for their paper. However, their Fig. 2 shows a latitude of between 23.8° and 24.0°N and an east longitude of between 342.5 and 343.0°E at 210 km altitude—while the entry state gives a latitude of 23 ± 0.04°N and an east longitude of 343.67 ± 0.01°E. This appears to us to be an inconsistency within Magalhães et al., regardless of any of our trajectory reconstruction work. This offset is of the

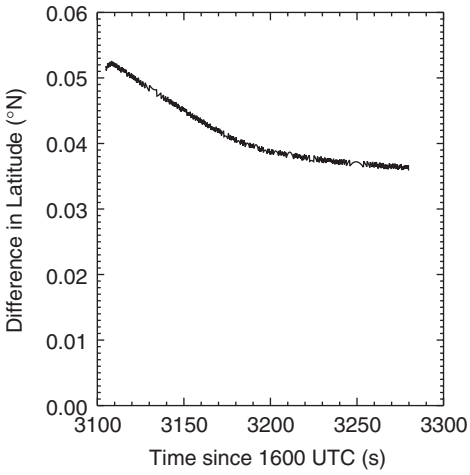

Fig. 3. Derived Pathfinder latitude subtracted from the PDS reconstructed latitude using the engineering entry state as a basis.

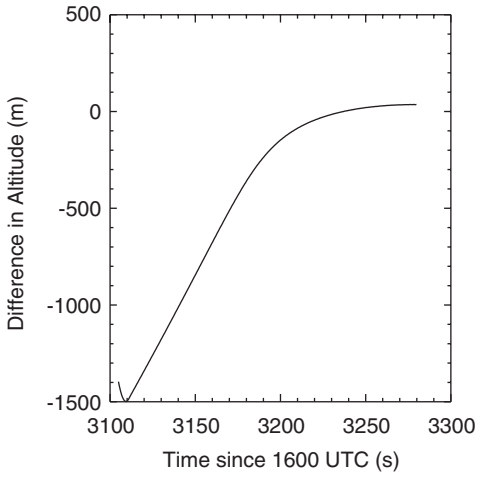

Fig. 5. As in Fig. 3, but altitude.

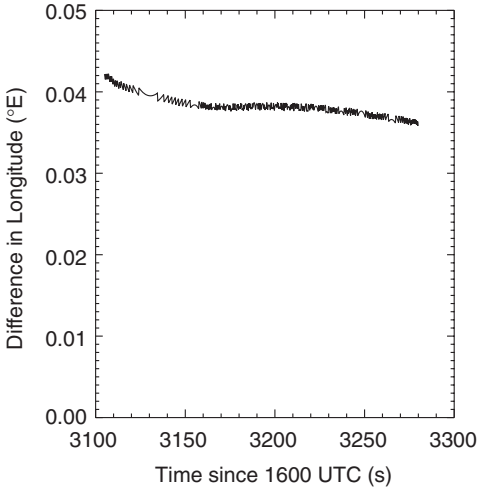

Fig. 4. As in Fig. 3, but east longitude.

same size and in the same direction as the offset between our reconstructed trajectory and the PDS values.

If we instead use the engineering entry state at 130 km altitude from Spencer et al. (1999), the systematic offset between our reconstructed trajectory and the PDS trajectory reduces to a few hundredths of a degree in both latitude and east longitude, as shown in Figs. 3 and 4, which is comparable with the likely uncertainties in latitude and east longitude in the engineering entry state. We assume that the uncertainties in the engineering entry state will be comparable to the uncertainties in the PDS entry state, since both are derived from the same tracking data.

We have taken the engineering entry state and integrated its trajectory backwards in time under the influence of gravity only. Under visual inspection, it appears identical to Fig. 2 of Magalhães et al. and hence does not pass through the position quoted as the PDS entry state. At the time of the engineering entry state, the position of the engineering entry state differs from that of the PDS trajectory by only $\sim 0.1^\circ$ in latitude and east longitude.

A reviewer has pointed out that the engineering entry speed is slower than the PDS entry speed, despite being at a lower altitude. Before significant atmospheric deceleration occurs, the spacecraft should speed up as it approaches Mars due to the attraction of martian gravity. This is another inconsistency between the engineering and PDS entry states.

We conclude that there is an error in Magalhães et al. (1999), most likely in the entry state. This error is probably present in the PDS archive as well. We have not been able to contact Julio Magalhães to discuss this as he is no longer active in planetary science. One of the other authors of Magalhães et al. (1999) is deceased and the other was not actively involved in this portion of their published research. Considering these inconsistencies, we elected to use the engineering entry state in our trajectory integration. Since the engineering entry state occurs at a later time than the PDS entry state, we again discard any accelerometer measurements that preceded it.

4.4. Results

Using the engineering entry state, the trajectory reconstruction results, shown in Figs. 3–5, are of good quality. Differences in latitude and east longitude between our values and the PDS data are on the order of a few hundredths of a degree. Differences in altitude are less than the uncertainty quoted for the PDS entry state and are on the order of a percent. We attribute the systematic offset in latitude and east longitude to the fact that the PDS trajectory is shifted to reproduce the landed position (Magalhães et al., 1999). We do not have a convincing explanation for the diminishing offset in altitude.

Continuing the trajectory through the parachute phase, our position at the time of landing is 502.7 m altitude below a reference radius of 3389.715 km, 19.054°N latitude,

and 326.445°E longitude. The PDS landed position is at the reference radius of 3389.715 km, 19.09°N latitude, and 326.48°E longitude.

Note that these results have been achieved without using any sophisticated aerodynamics.

5. Atmospheric structure reconstruction

5.1. Fluid dynamics during an atmospheric entry

For any given direction which may be related either to the *spacecraft* frame or to the direction of the fluid velocity, the aerodynamic force, F_{aero}, acting on the spacecraft can be expressed as follows:

$$F_{\text{aero}} = \frac{-\rho C A V^2}{2} = ma. \tag{18}$$

This is simply the result of a dimensional analysis of the problem, with the factor of two used by convention. All of the dependences on the body's shape, orientation, fluid composition, fluid temperature, and so on are hidden away in the dimensionless force coefficient C. If the chosen direction is parallel to the spacecraft's velocity with respect to the atmosphere, C is the drag coefficient and is often labelled with a subscript D. If the chosen direction is in the plane defined by the spacecraft's velocity with respect to the atmosphere and the direction of gravity and is also perpendicular to the spacecraft's velocity with respect to the atmosphere, C is the lift coefficient and is often labelled with a subscript L. Similarly, if the chosen direction is perpendicular to the drag and lift forces, C is the side force coefficient and is often labelled with a subscript Y. If the spacecraft is axisymmetric and the chosen direction is parallel to this axis, C is the axial force coefficient and is often labelled with a subscript A. If the chosen direction is perpendicular to this axis, C is the normal force coefficient and is often labelled with a subscript N. To emphasise that this force balance can be applied to any chosen direction, we retain the general force coefficient C rather than working with the common special cases of either the drag coefficient C_{D} or normal force coefficient C_{N}.

Changes in the spacecraft's speed and the atmosphere's physical properties during an atmospheric entry affect the spacecraft's aerodynamics. Here we outline the different aerodynamic regimes important for an atmosphere-entering spacecraft. We focus on the most important physical phenomena rather than on the exact numerical values of the force coefficients, and we do not discuss changes in a given force coefficient with changes in spacecraft attitude. See Vinh et al. (1980) for a discussion of this. We emphasise the drag coefficient since this is usually the most useful of the force coefficients.

The Navier–Stokes equation for the conservation of linear momentum in a continuum fluid can be written as (Faber, 1995):

$$\rho\left[\frac{\partial \underline{v}}{\partial t} + (\underline{v}\cdot\underline{\nabla})\underline{v}\right] = -\underline{\nabla} p - \underline{\nabla}\times(\eta\underline{\nabla}\times\underline{v}), \tag{19}$$

where η is the dynamic viscosity of the fluid. In the rest frame of a spacecraft in a planetary atmosphere, the spacecraft can be considered as an immersed object around which the continuum fluid must flow. This equation must be satisfied throughout the fluid and boundary conditions applied at the spacecraft–fluid interface.

By expressing each quantity in this equation (say x) in terms of the product of a characteristic value for that quantity (x_0) and a dimensionless number (x'), the equation can be rearranged to yield:

$$\rho'\left[\frac{\partial \underline{v}'}{\partial t'} + (\underline{v}'\cdot\underline{\nabla}')\underline{v}'\right] = -\left(\frac{p_0}{\rho_0 v_0^2}\right)\underline{\nabla}' p' - \left(\frac{\eta_0}{\rho_0 L_0 v_0}\right)\underline{\nabla}'(\eta'\underline{\nabla}'\times\underline{v}'). \tag{20}$$

The spatial derivative, $\underline{\nabla}$, is expressed as $\underline{\nabla}'/L_0$. The first ratio of characteristic values in parentheses is related to the Mach number, Ma, which is defined as the ratio of the characteristic speed to the speed of sound. For an ideal gas, the speed of sound is given by $(\gamma_{\text{fluid}}\, p/\rho)^{1/2}$ where γ_{fluid} is the ratio of specific heats of the fluid (e.g. Landau and Lifshitz, 1959). Hence this first ratio is $1/\gamma_{\text{fluid}}Ma^2$. Note that it contains a dependence on the composition of the fluid through γ_{fluid}. The second ratio of characteristic values in parentheses is defined as the reciprocal of the Reynolds number, Re. Physically different situations have identical dimensionless solutions for this equation if they have the same Re, Ma, and dimensionless boundary conditions (e.g. Bertin and Smith, 1979). This means that the aerodynamic behaviour of a large spacecraft under a specified atmospheric composition, density, and temperature can be studied experimentally with small-scale models immersed in a fluid of different density or temperature. This is significantly easier than building a wind tunnel large enough to contain a full-size spacecraft, capable of generating many different flow speeds, and able to be filled with a range of gases, such as CO_2 for Mars, N_2 for Titan, and H_2 for Jupiter, with various densities.

We first consider small Ma for which the fluid is incompressible. For small Re where viscous forces dominate over inertial forces, Stokes drag causes values of the drag coefficient far exceeding unity and inversely proportional to Re (e.g. Faber, 1995). As Re increases, the drag coefficient decreases towards values near unity. This increase in Re confines the effects of viscosity to a thin layer, the boundary layer, near the surface of the body. Flow is at first laminar within the boundary layer (e.g. Bertin and Smith, 1979). The bulk of the fluid behaves as if it were inviscid. As Re increases further, the flow within the boundary layer becomes turbulent, which decreases the drag, and the boundary layer separates from the surface, which increases the drag (e.g. Faber, 1995). Which of these two transitions occurs first and which dominates depends on the specific situation under consideration. For the idealised case of a perfectly inviscid

fluid and infinite *Re*, there should be no forces on the spacecraft at all; however, for a vanishingly small viscosity, or large *Re*, there is still appreciable resistance to flow. Flow at low *Re* is laminar, flow at high *Re* is turbulent and this fact is not dependent on *Ma* (e.g. Owczarek, 1964).

This picture is modified as *Ma* increases and the fluid becomes more compressible, which means that work can be done upon it. Variations in temperature within the fluid become large enough that heat transfer is important and the conservation of energy must be considered in constructing equations to describe the flow (e.g. Owczarek, 1964). This extra conservation law, which is considered simultaneously with the conservation of momentum, alters the behaviour of the flow and the force coefficients. A flow in which *Ma* is everywhere less than one is called subsonic. A transonic flow contains regions where *Ma* is less than one and where *Ma* is more than one; theoretical models of transonic flow are challenging as they include both subsonic and supersonic regimes. Flow in which *Ma* is everywhere greater than 1 is supersonic, whereas hypersonic flow is a supersonic flow in which the fluid cannot be treated as an ideal gas, either because it becomes dissociated, is no longer in thermodynamic equilibrium, or for some other reason. A working definition of hypersonic flow is $Ma > 5$.

A thermal boundary layer develops in compressible flows, similar to the viscous boundary layer, within which the effects of compressibility and heat transfer are confined (e.g. Owczarek, 1964). This affects the flow of the fluid and the force coefficients. In regions of the fluid where the flow is supersonic, shock waves develop across which thermodynamic and flow properties can be discontinuous. Interactions between the boundary layer and shock waves, which also alter the drag, become more important as *Ma* increases and the shock waves approach closer to the spacecraft's surface and the boundary layer. At hypersonic speeds, the effects of viscosity and compressibility are important throughout the shocked region of the flow, rather than being confined to boundary layers (e.g. Owczarek, 1964). At hypersonic speeds, it is a reasonable approximation to consider the force coefficients independent of *Ma* and *Re* (e.g. Vinh et al., 1980).

If gradients in thermodynamic properties are shorter than the mean free path of molecules within the fluid, or equivalently, if a molecule is more likely to collide with the spacecraft than with another molecule, then the continuum fluid model does not apply (Bird, 1994). The Knudsen number, *Kn*, defined as the ratio of the mean free path of molecules within the fluid to the characteristic length, is useful here. Using the kinetic theory of gases, $Ma/Re \sim Kn/\gamma_{\text{fluid}}^{1/2}$ (e.g. Owczarek, 1964). If *Kn* is less than 0.01, then continuum flow applies. In this limit, the fluid adjacent to the spacecraft surface is at rest with respect to it. As molecular collisions become less frequent, the fluid adjacent to the spacecraft surface can acquire some tangential velocity with respect to it. This intermediate regime, $0.01 < Kn < 1$, is the transitional flow regime. Finally, as the effects of molecule–molecule collisions become insignificant compared to those of spacecraft–molecule collisions, the free-molecular flow regime with $Kn > 1$ is entered. In this regime, molecules hitting the spacecraft reflect somewhere between specularly and diffusely with an energy that is somewhere between their energy upon hitting the surface and the thermal energy of the spacecraft's surface temperature (Bird, 1994). Chemical reactions are also possible between the spacecraft and impinging molecules.

The stated boundaries of the various flow regimes for *Ma* and *Kn* are not absolute. A single value for *Ma* or *Kn* may be appropriate for most of the flow, but there will always be some regions of the flow where local values of these dimensionless numbers differ significantly from the mean value. The shape of the spacecraft has an effect on precisely where these boundaries are. The composition of the fluid is important in most flow regimes because it affects the partition of energy between kinetic and internal (e.g. vibrational) modes and how the disturbed fluid returns to thermodynamic equilibrium (Bird, 1994). This, in turn, will affect the transfer of momentum and energy between the spacecraft and the fluid. There is also the possibility of chemical reactions in the disturbed fluid, which will change its physical properties, or between the fluid and the spacecraft, which may affect the drag. Ablation or thermal expansion of the spacecraft can also affect the drag. As an extreme example, consider an ice spacecraft. This will rapidly melt upon entry. Real spacecrafts are not made of ice, but none of them have the idealised physical properties of a perfectly rigid, inert body.

Continuum flow can be studied experimentally, such as in wind-tunnel experiments (Intrieri et al., 1977), or in numerical models such as HALIS or LAURA (Gnoffo et al., 1996). Rarefied flow is much harder to study experimentally (Blanchard et al., 1997). It can be modeled numerically with direct simulation Monte Carlo (DSMC) methods (Bird, 1994). Comparison to Viking flight data and ground-based validation experiments shows that the DSMC methods are accurate (Blanchard et al., 1997).

Pathfinder, which is a typical planetary lander or entry probe, experienced free-molecular flow upon first entering the martian atmosphere. This was followed by transitional flow, hypersonic continuum flow, and transonic continuum flow before its parachute was released for subsonic continuum flow (Magalhães et al., 1999). The drag coefficient was constant and about 2 in free-molecular flow. It decreased during the transitional flow regime, but remained relatively stable during the hypersonic continuum flow regime. It then changed more rapidly in the transonic continuum flow regime. The opening of the parachute changed the aerodynamic properties of the spacecraft immensely. The drag coefficient will behave similarly for other typical atmospheric entries. We do not generalise further about the behaviour of the drag coefficient during an atmospheric entry because it is so dependent on the shape of the spacecraft. Discussions relevant to specific spacecraft can be found in the literature.

5.2. Generalised density reconstruction

With the exception of the *acceleration ratios* option discussed earlier in Section 3.5, this takes place separately from the trajectory reconstruction. It uses the results of the trajectory reconstruction.

Putting the *measured* aerodynamic accelerations aside initially, the results of the trajectory reconstruction, spacecraft mass, size, and shape, and an *assumed* profile of atmospheric density and pressure are sufficient information for the aerodynamic database to *predict* the aerodynamic forces and torques at each point along the reconstructed trajectory. The specific results that are used from the trajectory reconstruction are spacecraft attitude with respect to the fluid velocity and the fluid speed.

For the chosen direction, Eq. (18) can then be trivially rearranged to give

$$C_{\text{estimated}} = \frac{-2F_{\text{aero,predicted}}}{\rho_{\text{assumed}} A V^2}, \tag{21}$$

which can then be solved to find $C_{\text{estimated}}$ at each point along the trajectory. C is a slowly varying function of the density and pressure of the atmosphere; so an *estimate* of C with an *assumed* density and pressure should be reasonably accurate for the *actual* state of the atmosphere. Reintroducing the measured aerodynamic accelerations, and treating C as known and ρ as unknown, can provide an *estimate* of atmospheric density at each point along the profile:

$$\rho_{\text{estimated}} = \frac{-2ma}{C_{\text{estimated}} A V^2}. \tag{22}$$

If this *estimate* agrees with the *assumed* value (which was needed to find $C_{\text{estimated}}$), then this density value is the *actual* atmospheric density. The *estimated* value is typically closer to the *actual* value than the initially *assumed* value is; so the *assumed* profile is replaced by the *estimated* profile and the whole process can be repeated iteratively until *assumed* (input) and *estimated* (output) profiles converge satisfactorily on the *actual* profile. Only a small number of iterations is usually needed (Magalhães et al., 1999). Magalhães et al. chose a direction parallel to the spacecraft's velocity with respect to the atmosphere for the drag direction, and used a constant value of C in their first iteration. C changes by only tens of percent for many orders of magnitude change in density and pressure. If C were not such a weak function of density and pressure, then convergence could not be guaranteed. Similar procedures can be implemented for a total of three linearly independent axes for both force balances and torque balances. This gives six estimates for density at each point along the profile, all of which should be consistent. In practice, uncertainties on the force balance along the axis closest to the flow direction are much lower than on the others; so this estimate is used alone.

This process is a pointwise solution procedure applied along the trajectory, and does not integrate densities from one timestep to the next. The term A is a reference area included to make C dimensionless, but it may or may not be the most obvious area one might select as a reference. Both A and m may change along the trajectory due to, for example, heat shield ablation. If this is likely, then additional measurements will be needed to constrain these values during the atmospheric entry. Modeling to predict F should of course use the appropriate values of A.

5.3. Generalised pressure and temperature reconstruction

An inviscid fluid, such as a planetary atmosphere, satisfies Euler's equation (Houghton, 2002):

$$\frac{\nabla p}{\rho} - \underline{g} + (\underline{v} \cdot \nabla)\underline{v} + \frac{\partial \underline{v}}{\partial t} = 0. \tag{23}$$

In the radial direction, the latter two terms (which are due to atmospheric motions) are much smaller than the first two terms, and so the equation of hydrostatic equilibrium applies (Holton, 1972):

$$\frac{\mathrm{d}p}{\mathrm{d}r} = \rho g_r. \tag{24}$$

Note that g_r is negative. It is usually also assumed that the horizontal extent of the entry trajectory is small enough that the pressure at a given altitude does not change significantly over that extent. This is again neglecting atmospheric motions. The equation of hydrostatic equilibrium can be integrated to yield a pressure profile, but it needs a constant of integration. This can be ignored and set to zero at high altitude, but the resultant pressure profile will be an underestimate. If the actual pressure at the top of the density profile is 1, then the actual pressure n scale heights below is e^n. If the estimated pressure at the top of the density profile is mistakenly set to 0, then the estimated pressure n scale heights below is $\mathrm{e}^n - 1$. The fractional underestimate in the pressure n scale heights below is therefore e^{-n}. Two scale heights below the top of the density profile, the underestimate is 14%; four scale heights below it is reduced to 2%.

A better approach uses the fact that atmospheric density and pressure are both changing exponentially with height, but atmospheric temperature is only changing linearly with height. The ideal gas law is

$$p = \rho T \frac{k_{\mathrm{B}}}{m_{\text{mol}}}, \tag{25}$$

where T is temperature, k_{B} is Boltzmann's constant, and m_{mol} is the mean molecular mass. With an ideal gas equation of state and the assumption that both atmospheric mean molecular mass and temperature vary much more slowly with altitude than atmospheric density does, one has

$$\frac{\mathrm{d}\rho}{\rho} = \frac{\mathrm{d}p}{p}. \tag{26}$$

Substituting Eq. (26) into Eq. (24) gives

$$\frac{p}{\rho}\frac{\mathrm{d}\rho}{\mathrm{d}r} = \rho g_r, \tag{27}$$

$$p \frac{\mathrm{d}}{\mathrm{d}r}(\ln \rho) = \rho g_r. \tag{28}$$

This gives an estimate for the pressure at the top of the density profile, where $r = r_0$, that can be calculated from the density profile alone:

$$p(r_0) = \rho(r_0) g_r(r_0) \times \left(\frac{\mathrm{d}}{\mathrm{d}r} (\ln \rho) \Big|_{r_0} \right)^{-1}. \quad (29)$$

This can then be used as the boundary condition when integrating Eq. (24) to get the pressure profile:

$$p(r) = \rho(r_0) g_r(r_0) \times \left(\frac{\mathrm{d}}{\mathrm{d}r} (\ln \rho) \Big|_{r_0} \right)^{-1} + \int_{r_0}^{r} \rho(r) g_r(r)\, \mathrm{d}r. \quad (30)$$

Finally, the derived density and pressure profiles can be substituted into Eq. (25) to give the temperature profile.

Modelling and the final reconstructed temperature profile can be used to estimate how much uncertainty the isothermal and ideal gas assumptions introduce into the constant of integration. More complicated equations of state can be considered if desired, but planetary atmospheres are sufficiently rarefied when first detected by current accelerometers that an ideal gas equation of state is very accurate.

5.4. Error considerations

The inaccuracies in the trajectory reconstruction affect the aerodynamic modelling and contribute to errors in C. However, C is also affected by intrinsic uncertainties in the aerodynamic modelling. These uncertainties in C, in the trajectory reconstruction (V), and in the measured accelerations then contribute to errors in the estimated value for ρ at each point along the trajectory. Errors in p are introduced by the assumption of a static atmosphere, by uncertainties in ρ, and by uncertainties in the gravitational field at the inaccurately known position of each point along the trajectory. Errors in T come from uncertainties in the atmospheric composition, ρ, p, and an assumed equation of state. As discussed in Section 6.3, errors in temperature can be significantly less than those in pressure and density.

Direct measurements of atmospheric properties including density, pressure, temperature, and wind velocity can improve the atmospheric structure reconstruction (Seiff and Kirk, 1977), while mass spectrometer measurements of atmospheric composition can yield an independent profile of atmospheric density (Nier and McElroy, 1977).

6. Atmospheric structure reconstruction applied to Mars Pathfinder

6.1. The importance of an aerodynamic database

As discussed in Section 4.1, we did not use the Moss et al. (1998) and Gnoffo et al. (1996) aerodynamic database for Pathfinder. Instead, we used Fig. 3 of Magalhães et al. (1999) which shows a profile of C_D as a function of altitude *as appropriate to their trajectory reconstruction*. We scanned and digitised this figure, then used this vertical profile of C_D as our aerodynamic database. If our trajectory reconstruction has a different speed at a given altitude than theirs, then we are forced to use the value of C_D appropriate to their speed. This is a source of error, but since our trajectory reconstruction is reasonably close to theirs, we believe that the major source of error is in the crude scanning and digitisation.

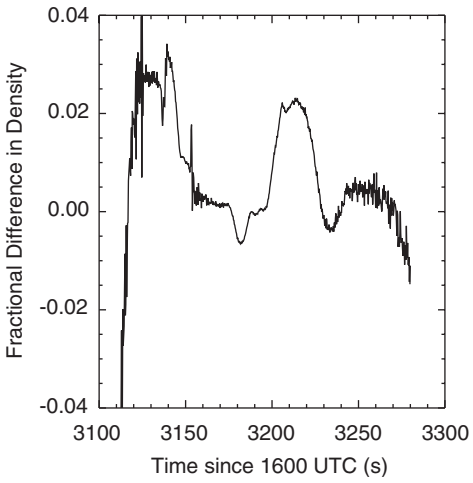

Fig. 6. The ratio of (PDS reconstructed density minus the results of this paper using the engineering entry state) to the PDS reconstructed density, plotted against the independent variable time.

6.2. Results

As stated in the PDS file /document/edlddrds.htm, the spacecraft reference area, A, is 5.526 m^2 and its mass, m, is 585.3 kg. These, the results of the trajectory reconstruction, and our crude aerodynamic database are all that is needed to derive the profile of atmospheric density. For the constant of integration in the equation of hydrostatic equilibrium, we estimated the density scale height over the uppermost 10 km of the density profile and assigned this value to the altitude in the midpoint of this range. We used a spherically symmetric gravitational field and numerically integrated the equation of hydrostatic equilibrium. Uncertainties due to the crude aerodynamic database dwarf the neglected effects of higher order terms in the gravitational field.

The mean molecular mass assumed in the ideal gas equation of state was 43.49 g mol^{-1} in the lower atmosphere, and decreased with altitude as discussed in Magalhães et al. (1999) and tabulated in PDS file /document/edlddrds.htm.

As a function of the independent variable in the reconstruction, time, the density, pressure, and temperature results, shown in Figs. 6–8 are consistent to within a few percent. When more usefully plotted against reconstructed

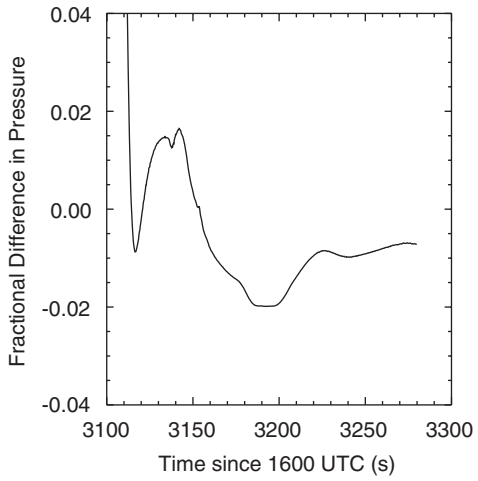

Fig. 7. As in Fig. 6, but pressure.

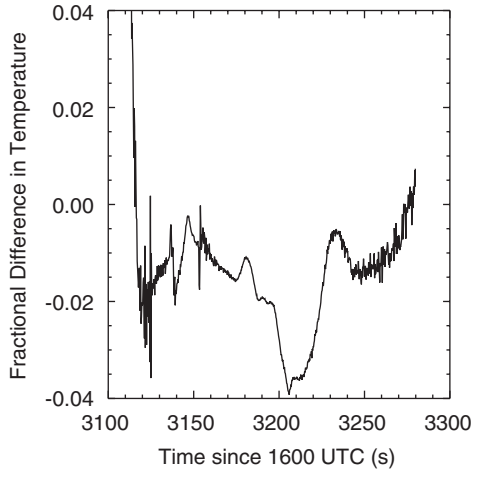

Fig. 8. As in Fig. 6, but temperature.

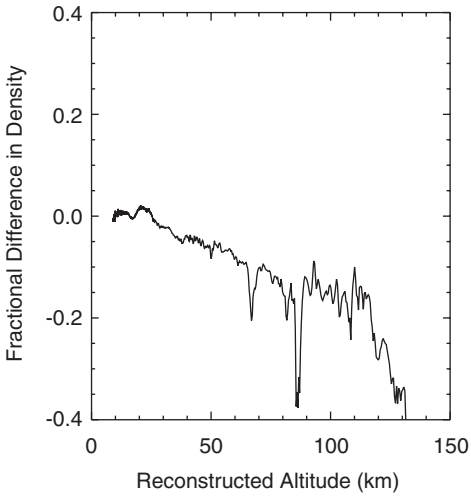

Fig. 9. The ratio of (PDS reconstructed density minus the results of this paper using the engineering entry state) to the PDS reconstructed density, plotted against reconstructed altitude.

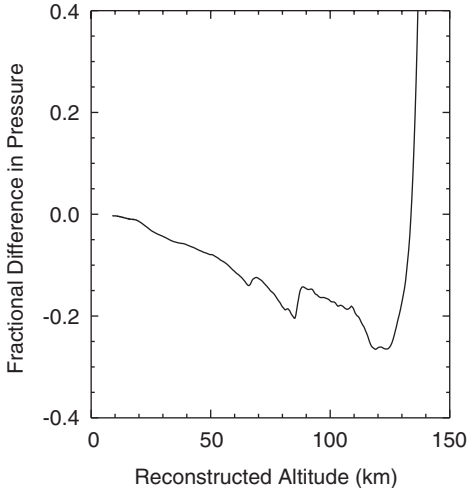

Fig. 10. As in Fig. 9, but pressure.

altitude in Figs. 9–11, the density and pressure results are only consistent to 20% or so. This apparent worsening of our results is due to differences between our profile of reconstructed altitude versus time and that of the PDS. However, the temperature versus reconstructed altitude results are still consistent to about 5%. Sudden jumps in the difference between our results and the PDS results at 85 and 65 km altitude occur at changes in accelerometer gain state. We believe that the PDS has used a different interpolation technique to ourselves to replace the corrupted second of data.

6.3. $C_D = 2$ *approximation*

In sufficiently rarefied atmospheres, i.e. at sufficiently high altitudes, the motions of atmospheric molecules are not affected by those of other molecules. In this situation, atmospheric molecules below the spacecraft are dynamically unaware of its impending arrival and are accelerated from near-zero thermal speeds to the kilometre per second-scale entry speed of the spacecraft as they are physically swept up by its passage. The spacecraft sweeps through a volume of atmosphere Av per unit time. It accelerates the mass ρAv of this volume to a speed v. The momentum transferred by the spacecraft to the atmosphere per unit time is therefore ρAv^2. This is the force exerted parallel to the velocity of the spacecraft with respect to the atmosphere and so, by reference to Eq. (17), C for this direction should be 2. This is C_D, the drag coefficient. C_D does not change by orders of magnitude during an atmospheric entry, only by tens of percent. This is many times less than the acceleration and velocity, the other terms which change in Eq. (17) to affect the measurement of atmospheric density.

$C_D = 2$ might be used as a default aerodynamic database in the unfortunate case where no aerodynamic information

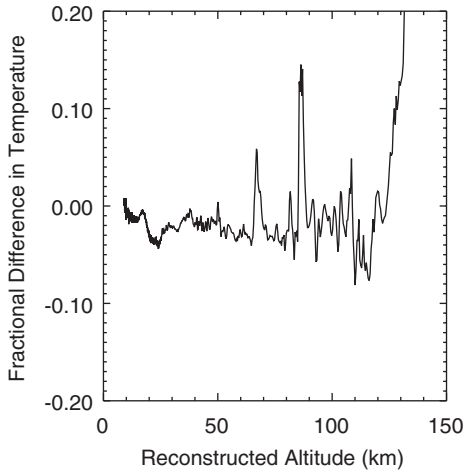

Fig. 11. As in Fig. 9, but temperature.

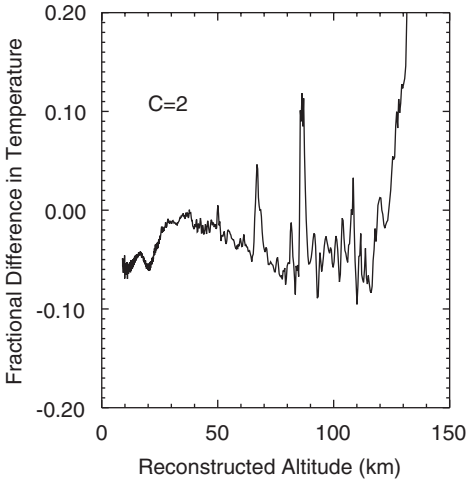

Fig. 12. The ratio of (PDS reconstructed temperature minus the results of this paper using the engineering entry state and taking $C = 2$) to the PDS reconstructed temperature, plotted against reconstructed altitude.

is available or when a very rapid atmospheric characterisation is required. We plot temperature as a function of reconstructed altitude in Fig. 12 using this approximation. The error increases from about 4% (variable C_D) to about 8% ($C_D = 2$), which is a remarkably accurate result considering how much time-consuming and expensive aerodynamic modelling has been neglected. The fractional error in density, not shown, is equal to the negative fractional difference between the actual and assumed values of C_D. Gravity is nearly constant over the altitude range of atmospheric entry, so pressure is effectively proportional to the integral of density with respect to altitude. Since density is inversely proportional to C_D, and C_D changes slowly with altitude, the ratio of pressure to density is only slightly dependent on C_D. Using the ideal gas equation of state, temperature is proportional to the ratio of pressure to density and also only slightly dependent on C_D. Hence errors in C_D, which may be very important for the density or pressure results, cause the uncertainty in the temperature results to increase by only a few percentage points.

Two effects are important in understanding why temperature is so weakly dependent on C_D. Neither of them alone is sufficient. First, C_D varies by only tens of percent during atmospheric entry. Second, temperature is proportional to a ratio between an integration of C_D^{-1} over altitude and C_D^{-1}, not directly to C_D.

7. Conclusions

We have developed procedures to analyse accelerometer data for trajectory and atmospheric structure reconstruction and outlined them in detail. Different approaches to the problem of tracking spacecraft attitude have been compared and contrasted. Our trajectory reconstruction procedures have been verified on the Pathfinder entry. They have uncovered inconsistencies within the previously published work, including the PDS archive. The iterative approach needed to obtain an accurate atmospheric density profile and the pointwise nature of the procedure have been emphasised in our outline of the theory of atmospheric structure reconstruction. Our atmospheric structure reconstruction results have been verified on the Pathfinder entry using a very crude aerodynamic database. The results for both the trajectory and atmospheric structure reconstructions are good, and in fact a remarkably accurate profile of atmospheric temperature may be obtained without any aerodynamic database whatsoever. Our trajectory reconstruction procedures may need to be modified for application to an entry probe into a satellite's atmosphere, such as Huygens. The parent planet's gravitational attraction may be strong enough that it needs to be included in the trajectory reconstruction in addition to the satellite's gravity. For an entry of short duration, the planet's gravitational attraction should be constant in an inertial frame.

As a service to the community, we have placed simplified versions of our trajectory and atmospheric structure computer programmes online for public use. Interested parties should contact the authors, who will be happy to provide them with further details. Currently, the online programmes assume a spherically symmetric planet and gravitational field, use only a first-order integration technique and model spacecraft aerodynamics with constant C and the *head-on* or *drag-only* options. However, it is our intent to further develop them for application to upcoming planetary missions.

Acknowledgements

Atmospheric structure reconstruction from planetary entry accelerometer data was pioneered by Al Seiff and this paper owes much to his ideas and achievements (Young and Magalhães, 2001). This work was performed whilst PW was

a consultant at the Open University. We acknowledge helpful discussions with Dave Atkinson, Ralph Lorenz, and Bob Tolson.

References

Arfken, G.B., Weber, H.J., 1995. Mathematical Methods for Physicists. Academic Press, San Diego, CA, USA.

Avduevskii, V.S., Godnev, A.G., Semenchenko, V.V., Uspenskii, G.R., Cheremukhina, Z.P., 1983a. Investigation of the characteristics of the Venus stratosphere from acceleration measurements during the braking of the Venera-13 and Venera-14 probes. Cosmic Res. 21, 205–210.

Avduevskii, V.S., Marov, M.Ia., Kulikov, Iu.N., Shari, V.P., Gorbachevskii, A.Ia., Uspenskii, G.R., Cheremukhina, Z.P., 1983b. Structure and parameters of the Venus atmosphere according to Venera probe data. In: Hunten, D.M., Colin, L., Donahue, T.M., Moroz, V.I. (Eds.), Venus. University of Arizona Press, Tucson, AZ, USA, pp. 280–298.

Bendura, R.J., Lundstrom, R.R., Renfroe, P.G., 1974. Flight Tests of Viking Parachute System in Three Mach Number Regimes. 2: Parachute Test Results. NASA-TN-D-7734. Langley Research Center, Virginia, USA.

Bertin, J.J., Smith, M.L., 1979. Aerodynamics for Engineers. Prentice-Hall, New Jersey, USA.

Bird, G.A., 1994. Molecular Gas Dynamics. Clarendon Press, Oxford, UK.

Blanchard, R.C., Hinson, E.W., Nicholson, J.Y., 1989. Shuttle high-resolution accelerometer package experiment results—atmospheric density measurements between 60 and 160 km. J. Spacecraft Rockets 26 (3), 173–180.

Blanchard, R.C., Wilmoth, R.G., Moss, J.N., 1997. Aerodynamic flight measurements and rarefied-flow simulations of Mars entry vehicles. J. Spacecraft Rockets 34 (5), 687–690.

Braun, R.D., Spencer, D.A., Kallemeyn, P.H., Vaughan, R.M., 1999. Mars Pathfinder atmospheric entry navigation operations. J. Spacecraft Rockets 36 (3), 348–356.

Croom, C.A., Tolson, R.H., 1994. Using Magellan attitude control data to study the Venusian atmosphere and various spacecraft properties. Adv. Astronaut. Sci. 87, 451–467.

Faber, T.E., 1995. Fluid Dynamics for Physicists. Cambridge University Press, UK.

Gnoffo, P.A., Weilmuenster, K.J., Braun, R.D., Cruz, C.I., 1996. Influence of sonic-line location on Mars Pathfinder probe aerothermodynamics. J. Spacecraft Rockets 33 (2), 169–177.

Goldstein, H., 1980. Classical Mechanics, 2nd Edition. Addison-Wesley Pub. Co., Reading, MA, USA.

Golombek, M., Cook, R.A., Economou, T., Folkner, W.M., Haldemann, A.F.C., Kallemeyn, P.H., Knudsen, J.M., Manning, R.M., Moore, H.J., Parker, T.J., Rieder, R., Schofield, J.T., Smith, P.H., Vaughan, R.M., 1997. Overview of the Mars Pathfinder mission and assessment of landing site predictions. Science 278, 1743.

Golombek, M.P., 1999. Introduction to the special section: Mars Pathfinder. J. Geophys. Res. 104, 8521–8522.

Holton, J.R., 1972. An Introduction to Dynamic Meteorology. Academic Press, New York, USA.

Houghton, J.T., 2002. The Physics of Atmospheres. Cambridge University Press, UK.

Intrieri, P.F., Rose, C.E.D., Kirk, D.B., 1977. Flight characteristics of probes in the atmospheres of Mars, Venus and outer Planets. Acta Astron. 4 (7-8), 789–799.

Kaula, W.M., 1966. Theory of Satellite Geodesy; Applications of Satellites to Geodesy. Blaisdell Pub. Co., Waltham, MA, USA.

Keating, G.M., Bougher, S.W., Zurek, R.W., Tolson, R.H., Cancro, G.J., Noll, S.N., Parker, J.S., Schellenberg, T.J., Shane, R.W., Wilkerson, B.L., Murphy, J.R., Hollingsworth, J.L., Haberle, R.M., Joshi, M., Pearl, J.C., Conrath, B.J., Smith, M.D., Clancy, R.T., Blanchard, R.C., Wilmoth, R.G., Rault, D.F., Martin, T.Z., Lyons, D.T., Esposito, P.B., Johnston, M.D., Whetzel, C.W., Justus, C.G., Babicke, J.M., 1998. The structure of the upper atmosphere of Mars: in situ accelerometer measurements from Mars global surveyor. Science 279, 1672–1676.

Kerzhanovich, V.V., 1977. Mars 6—improved analysis of the descent module measurements. Icarus 30, 1–25.

Landau, L.D., Lifshitz, E.M., 1956. Statistical Physics. Pergamon Press, London, UK.

Landau, L.D., Lifshitz, E.M., 1959. Fluid Mechanics. Pergamon Press, London, UK.

Landau, L.D., Lifshitz, E.M., 1960. Mechanics. Pergamon Press, London, UK.

Lang, K.R., 1999. Astrophysical Formulae. Springer, New York, USA.

Lebreton, J.-P., Verdant, M., Wills, R.D., 1994. Huygens—the science, payload and mission profile. ESA Bull. 77, 31–41.

Lemoine, F.G., Smith, D.E., Rowlands, D.D., Zuber, M.T., Neumann, G.A., Chinn, D.S., Pavlis, D.E., 2001. An improved solution of the gravity field of Mars (GMM-2B) from Mars Global Surveyor. J. Geophys. Res. 106, 23359–23376.

Lodders, K., Fegley, B., 1998. The Planetary Scientist's Companion. Oxford University Press, UK.

Magalhães, J.A., Schofield, J.T., Seiff, A., 1999. Results of the Mars Pathfinder atmospheric structure investigation. J. Geophys. Res. 104, 8943–8956.

Marcos, F.A., Garrett, H.B., Champion, K.S.W., Forbes, J.M., 1977. Density variations in lower thermosphere from analysis of AE-C accelerometer measurements. Planet. Space Sci. 25 (5), 499–507.

Moss, J.N., Blanchard, R.C., Wilmoth, R.G., Braun, R.D., 1998. Mars Pathfinder rarefied aerodynamics: computations and measurements. American Institute of Aeronautics and Astronautics Paper 98-0298, Presented at the 36th AIAA Aerospace Science Meeting in Reno, Nevada, USA.

Nier, A.O., McElroy, M.B., 1977. Composition and structure of Mars upper atmosphere—results from neutral mass spectrometers on Vikings 1 and 2. J. Geophys. Res. 82, 4341–4349.

Owczarek, J.A., 1964. Fundamentals of Gas Dynamics. International Textbook Company, Pennsylvania, USA.

Peterson, V.L., 1965a. A technique for determining planetary atmosphere structure from measured accelerations of an entry vehicle. NASA TN D-2669. Ames Research Center, California, USA.

Peterson, V.L., 1965b. Analysis of the errors associated with the determination of planetary atmosphere structure from measured accelerations of an entry vehicle. NASA-TR-R-225. Ames Research Center, California, USA.

Seiff, A., 1963. Some possibilities for determining the characteristics of the atmospheres of Mars and Venus from gas-dynamic behavior of a probe vehicle. NASA TN D-1770. Ames Research Center, California, USA.

Seiff, A., Kirk, D.B., 1977. Structure of the atmosphere of Mars in summer at mid-latitudes. J. Geophys. Res. 82, 4364–4378.

Seiff, A., Reese, D.E., Sommer, S.C., Kirk, D.B., Whiting, E.E., Niemann, H.B., 1973. PAET: an entry probe experiment in the Earth's atmosphere. Icarus 18, 525–563.

Seiff, A., Kirk, D.B., Young, R.E., Blanchard, R.C., Findlay, J.T., Kelly, G.M., Sommer, S.C., 1980. Measurements of thermal structure and thermal contrasts in the atmosphere of Venus and related dynamical observations—results from the four Pioneer Venus probes. J. Geophys. Res. 85, 7903–7933.

Seiff, A, Kirk, D.B., Knight, T.C.D., Young, R.E., Mihalov, J.D., Young, L.A., Milos, F.S., Schubert, G., Blanchard, R.C., Atkinson, D., 1998. Thermal structure of Jupiter's atmosphere near the edge of a 5-μm hot spot in the north equatorial belt. J. Geophys. Res. 103, 22857–22889.

Sims, M.R., Pillinger, C.T., Wright, I.P., Dowson, J., Whitehead, S., Wells, A., Spragg, J.E., Fraser, G., Richter, L., Hamacher, H., Johnstone, A., Meredith, N.P., de La Nougerede, C., Hancock, B., Turner, R., Peskett,

S., Brack, A., Hobbs, J., Newns, M., Senior, A., Humphries, M., Keller, H.U., Thomas, N., Lingard, J.S., Underwood, J.C., Sale, N.M., Neal, M.F., Klingelhofer, G., Ng, T.C., 1999. Beagle 2: a proposed exobiology lander for ESA's 2003 Mars Express mission. Adv. Space Res. 23 (11), 1925–1928.

Smith, D.E., Lerch, F.J., Nerem, R.S., Zuber, M.T., Patel, G.B., Fricke, S.K., Lemoine, F.G., 1993. An improved gravity model for Mars—Goddard Mars-Model-1. J. Geophys. Res. 98, 20871–20889.

Sommer, S.C., Yee, L., 1969. An experiment to determine the structure of a planetary atmosphere. J. Spacecraft Rockets 6 (6), 704–710.

Spencer, D.A., Blanchard, R.C., Braun, R.D., Kallemeyn, P.H., Thurman, S.W., 1999. Mars Pathfinder entry, descent, and landing reconstruction. J. Spacecraft Rockets 36 (3), 357–366.

Squyres, S.W., 2001. The Mars Exploration Rover Project. American Geophysical Union, Fall Meeting, abstract #P41A-09.

Strangeway, R.J., 1993. The Pioneer Venus orbiter entry phase. Geophys. Res. Lett. 20, 2715–2717.

Tolson, R.H., Keating, G.M., Cancro, G.J., Parker, J.S., Noll, S.N., Wilkerson, B.L., 1999. Application of accelerometer data to Mars global surveyor aerobraking operations. J. Spacecraft Rockets 36 (3), 323–329.

Tu, K.Y., Munir, M.S., Mease, K.D., Bayard, D.S., 2000. Drag-based predictive tracking guidance for Mars precision landing. J. Guidance Control Dynamics 23 (4), 620–628.

Vinh, N.X., Busemann, A., Culp, R.D., 1980. Hypersonic and Planetary Entry Flight Mechanics. University of Michigan Press, USA.

Wercinski, P.F., Lyne, J.E., 1994. Mars aerocapture—extension and refinement. J. Spacecraft Rockets 31 (4), 703–705.

Young, R.E., Magalhães, J.A., 2001. Alvin Seiff (1922–2000). Icarus 152, 1–3.